UNIVERSITY OF CALIFORNIA
Los Angeles

Analysis and Synthesis of Flexure Systems via Screw Algebra and Graph Theory

A dissertation submitted in partial satisfaction of the
requirements for the degree Doctor of Philosophy
in Mechanical Engineering

by

Frederick Sun

2017

ABSTRACT OF THE DISSERTATION

Analysis and Synthesis of General Flexure Systems
via Screw Algebra and Graph Theory

by

Frederick Sun
Doctor of Philosophy in Mechanical Engineering
University of California, Los Angeles, 2017
Professor Jonathan Hopkins, Chair

This thesis introduces a general method for analyzing and synthesizing flexure systems of any configuration, including those that cannot be broken into parallel and serial subsystems. Such flexure systems are called interconnected hybrid flexure systems because they possess limbs with intermediate bodies that are connected by flexure systems or elements. Specifically, the method introduced utilizes screw algebra and graph theory to help designers determine the freedom spaces (i.e., the geometric shapes that represent all the ways a body is permitted to move) for all the bodies joined together by compliant flexure elements within interconnected hybrid flexure systems (i.e., perform mobility analysis of general flexure systems). This method also allows designers to determine (i) whether such systems are under-constrained or not and (ii) whether such systems are over-constrained or exactly-constrained (i.e., perform constraint analysis of general flexure systems). Although many flexure-based precision motion stages, compliant mechanisms, and microarchitectured materials possess topologies that are highly interconnected, the theory for

performing the mobility and constraint analysis and synthesis of such interconnected flexure systems using traditional screw theory does not currently exist. The theory introduced here lays the foundation for an automated tool that can rapidly generate the freedom spaces of every rigid body within a general flexure system without having to perform traditional computationally expensive finite element analysis. Case studies are provided to demonstrate the utility of the proposed theory.

The dissertation of Frederick Sun is approved.

Robert N. Candler

Veronica Santos

Dennis W. Hong

Jonathan B. Hopkins, Chair

University of California, Los Angeles, 2017

TABLE OF CONTENTS

LIST OF FIGURES

LIST OF TABLES

VITA

2007	B.S. (Mechanical Engineering), National University of Taiwan, Taipei, Taiwan, R.O.C.
2009	M.S. (Mechanical Engineering), National University of Taiwan, Taipei, Taiwan, R.O.C.
2009-2012	Engineer, Zoeller Taiwan Co., LTD.
2012-2017	Graduate Student, Mechanical and Aerospace Engineering Department, University of California, Los Angeles (UCLA), Los Angeles, CA
2014-2017	Teaching Assistant, Mechanical and Aerospace Engineering Department, University of California, Los Angeles (UCLA), Los Angeles, CA

CHAPTER 1

Introduction

Flexure systems [1] consist of rigid bodies, shown as rectangles in the schematic portion of Fig. 1.1, joined together by flexure elements (e.g., wire, blade, or notch flexures), shown as springs in the same portion, of Fig. 1.1, joined together by flexure elements (e.g., wire, blade, or notch flexures), shown as springs in the same portion, that deform to guide the system's rigid bodies along desired motion paths with high precision. According to their geometry, these elements are stiff in certain directions but compliant in other directions. The directions of greatest compliance exhibited by a body constrained by flexure elements within a flexure system are the body's degrees of freedom (DOFs). There are three kinds of rigid bodies within a flexure system—a grounded or fixed body labeled 'G' in Fig. 1.1, intermediate bodies labeled 'I', and a stage labeled 'S'. A system's stage is the primary body of interest (i.e., the body that performs the system's desired tasks).

Traditionally, flexure systems are classified into three categories [1,2] (Fig. 1.1)—parallel, serial, and hybrid. Parallel systems consist of two rigid bodies joined directly together by flexure elements as shown in the example of Fig. 1.1. Serial flexure systems consist of two or more parallel subsystems stacked or nested together in a chain-like configuration. Hybrid flexure systems consist of any other configuration of rigid bodies joined together by flexure elements. Most hybrid systems consist of various combinations of both parallel and serial subsystems joined together in parallel. Note that the hybrid system example in Fig. 1.1 consists of three identical serial subsystems or limbs arranged in

parallel, where the serial subsystems or limbs can be lumped to together into a kinematically equivalent subsystem, which is not always the case.

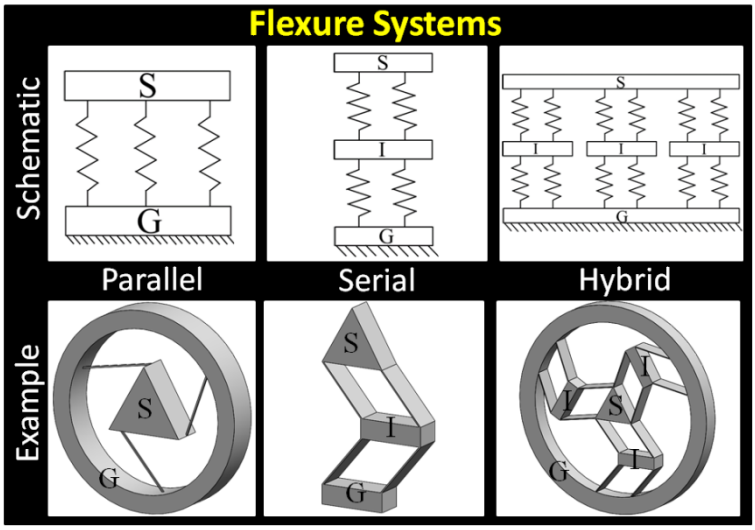

Figure 1.1: Flexure system categories

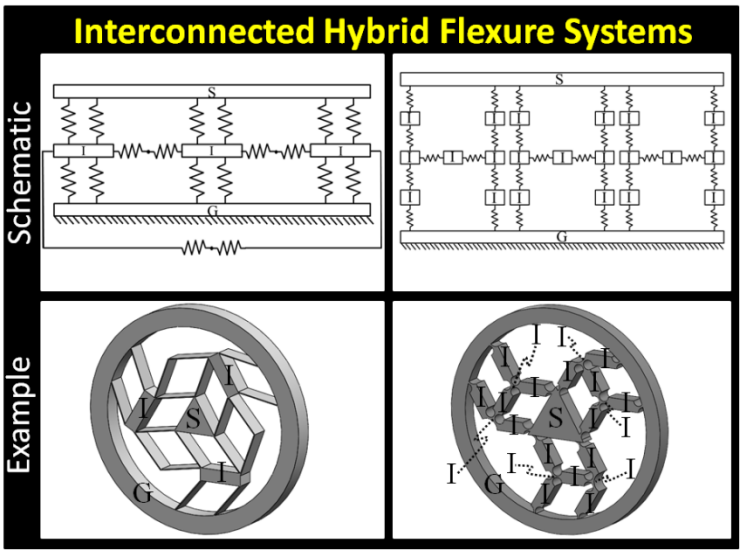

Figure 1.2: Interconnected hybrid system examples

Some hybrid flexure systems, however, are arranged in configurations that cannot be broken into purely parallel and serial subsystems. Two examples of this kind of hybrid system are shown in Fig. 1.2. These systems are called interconnected hybrid flexure systems [2] because they possess at least one set of parallel limbs that are interconnected by flexure subsystems or elements that join the limbs' intermediate bodies together. Screw-theory-based approaches can't traditionally be used to analyze or synthesize such interconnected hybrid systems because most existing approaches can only analyze or synthesize systems that can be broken into parallel and serial subsystems like the hybrid example of Fig. 1.1, and therefore cannot be analyzed or synthesized using the traditional FACT approach.

The purpose of this thesis is to introduce a new systematic analysis and synthesis approach for general interconnected hybrid flexure systems flexure systems. The method introduced can also determine whether such systems are under-constrained or not and whether such systems are exactly-constrained or over-constrained (i.e., constraint analysis). Since interconnected hybrid systems are the most complex class of system, this thesis will enable the general analysis and synthesis of flexure systems of any configuration.

The ability to analyze and synthesize interconnected hybrid flexure system designs is becoming increasingly important as more and more applications are emerging that require the use of such designs. Nano-positioners and other flexure-based motion stages, like those shown in the example portion of Fig. 1.2 for instance, require an interconnected hybrid flexure topology to simultaneously achieve their desired stage DOFs while also satisfying their desired load capacity, stiffness, and

dynamic requirements. Serial flexure systems that achieve large ranges of motion often suffer from under-constraint, which can be eliminated by the addition of flexure linkages [3] that render the system's topology interconnected. The topologies of repeating unit cells within periodic microarchitectured material lattices [4,5] are often interconnected hybrid in their configuration. Such material lattices, also called mechanical metamaterials [6], can be engineered to exhibit a large variety of tunable bulk properties (e.g., negative Poisson ratio [7], zero or negative thermal expansion coefficient [8], and high strength-to-weight ratio [5]), which are primarily determined by their microstructure's interconnected hybrid flexure topology.

The theory of this thesis uniquely utilizes a combination of screw algebra [9-11] and graph theory [12,13] to enable the analysis of interconnected hybrid flexure system topologies. Twist and wrench vectors [9-11] are used in the context of screw algebra to model the DOFs and the constraining forces imposed on the rigid bodies within a general flexure system. Graph theory is used to model the system's rigid bodies as nodes or vertices and flexure elements as edges within a graph to mathematically navigate the graph's complex connections to identify the fewest number of vector equations that need to be solved for completing the mobility analysis of the interconnected hybrid system.

Screw algebra has been used extensively by others to analyze the mobility of rigid mechanisms of various configurations for the past few centuries [9-11,14]. Screw systems that consist of linear combinations of twist and wrench vectors have been studied exhaustively and classified for a variety

of rigid mechanism purposes [15-19]. Mohamed and Duffy [20] investigated the instantaneous kinematics of a parallel manipulator with identical serial chain limbs. Kumar [21] used reciprocal twist and wrench vectors for instantaneous kinematic analysis of serial kinematic chains arranged in parallel. Kong and Gosselin [22,23] used wrenches to synthesize three DOF parallel manipulators. Fang and Tsai [24] synthesized parallel manipulators with identical limbs of four and five DOFs.

Graph theory has also been applied in conjunction with screw algebra to analyze and synthesize rigid mechanisms of various configurations. Freudenstein and Dobrjanskyj [25,26] used graph theory to model the links and joints of general rigid mechanisms as vertices and edges similar to the theory of this paper but utilized different mathematics to identify non-isomorphic graphs for the purpose of type synthesis for various types of mechanisms. Davies [27] applied Kirchhoff's voltage law to rigid mechanisms, treating closed kinematic chains as an analogue to closed electrical circuits. Angeles and Gosselin [28] addressed the mobility of multi-loop rigid mechanisms by calculating the nullity of a mechanism's Jacobian matrix. Zoppi et al. [29] analyze parallel manipulators with interconnecting links. Zeng et al. [30] designed a parallel manipulator that also possessed interconnecting links. Lu and Leinonen [31] used graph theory to synthesize a family of unified planar and spatial mechanisms. Chen and Yao [32] used graph theory to create a systematic approach for synthesizing the topology of fractionated geared differential mechanisms.

Although screw algebra and graph theory have been applied extensively to rigid mechanisms, the combination of these principles have not yet been commonly applied to compliant

mechanisms—particularly for solving the mobility of interconnected hybrid flexure systems. Murphy, et al. [33] included flexures as a type of joint to enumerating non-isomorphic compliant mechanisms. Pucheta and Cardona [34] applied graph theory to perform the type synthesis of compliant mechanisms that derive from rigid mechanism analogues. Adding to the contributions of Merlet [35] and Hao [36], Hopkins created the Freedom and Constraint Topologies (FACT) synthesis approach [37-39], which utilizes a comprehensive library of intuitive shapes, as shown in Fig. 1.3, that help designers leverage the geometry of screw systems toward visualizing the topologies and mobility of general compliant mechanisms. The mathematics underlying the FACT approach was furthered by Su et al. [40-42] and Yu et al. [43] to enhance the computational analysis and synthesis of flexure systems of various parallel and serial flexure configurations. Some approaches have also utilized screw algebra to analyze and synthesize compliant mechanisms [44,45]. More recently, an approach was created that normalizes the compliance matrices of flexure systems to identify the directions of greatest compliance (i.e., the DOFs) [46, 47]. Other approaches for analyzing and synthesizing compliant mechanisms and flexures have also been developed. Howell [48] developed the pseudo rigid body model to approximate large deformation of compliant mechanisms and flexures by replacing the flexible elements with traditional rigid body mechanism joints. Kota et al. [49] developed a computation based method that optimizes the geometry of a material to achieve desired output from input, and although the method is powerful it is also computational intensive.

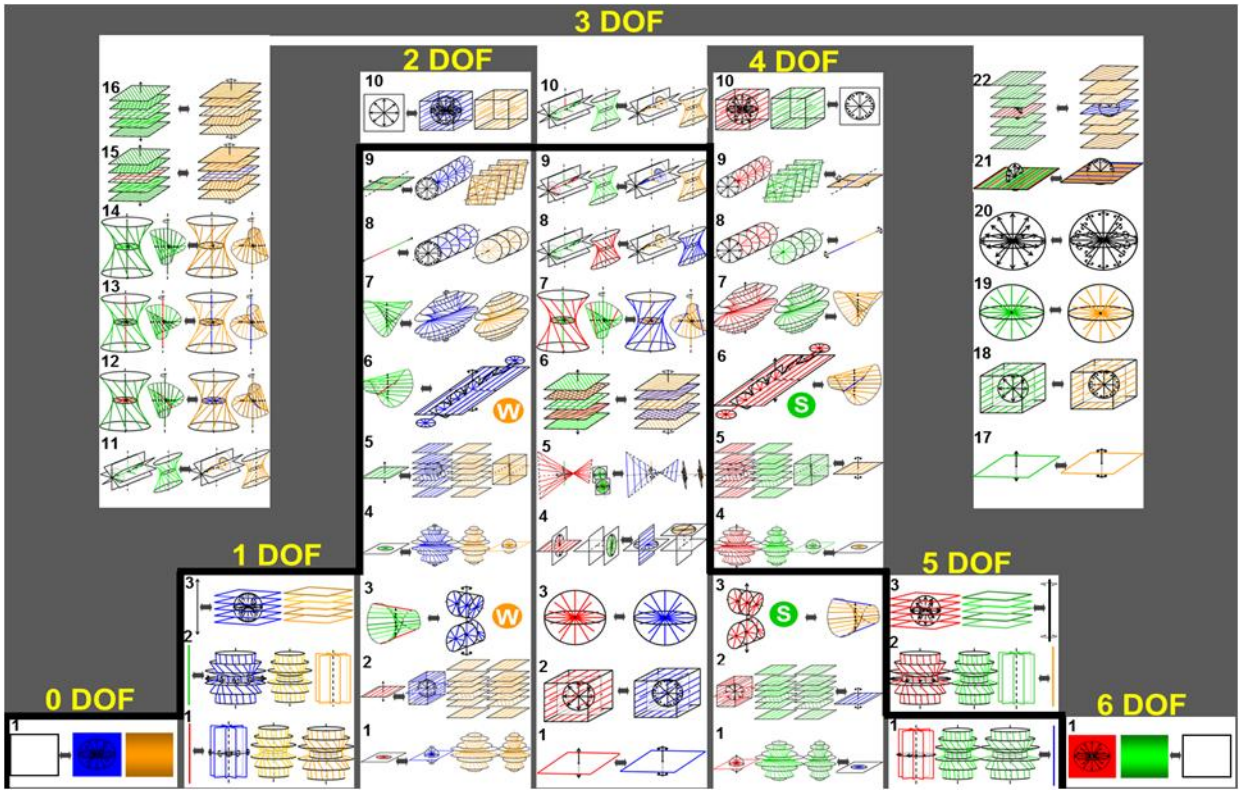

Figure 1.3: Mathematical complete FACT library [38]

The approach introduced in this work extends upon the FACT approach. The FACT approach offers the advantage of better precision in small deformation, it allows more human interaction in the process such that the design can be easier conceptualized, and the extension of FACT developed in this thesis also offers a basis that allows a more efficient automated design algorithm to be developed in the future. The FACT library in Fig.1.3 will be repeatedly used in chapter 3 and chapter for of this thesis. FACT is used to identify and interprets the motion of flexure elements into twist and wrench vectors for analysis, and conceptually design flexure elements when given twists and wrench vectors when performing synthesis. The approach however, does not use the traditional FACT approach that lumps the limbs broadens the scope of FACT, and enables the analysis and synthesis of any compliant

mechanism (both interconnected or not interconnected) in that it allows users to identify and specify the DOFs of

the rigid bodies within the mechanism regardless of how they are joined together by flexure elements, and synthesize flexure systems with any desired DOF regardless of how the rigid bodies are joined together. The approach is able to identify these DOFs rapidly in part because the calculations inherent to the approach only consider the topology of the system's flexure elements (i.e., the kind, location, and orientation of the elements within the system). The shapes of the rigid bodies, the properties of the constituent materials used, and the geometric parameters of the flexure elements (e.g., the lengths, widths, or thicknesses of rectangular prism elements) that make up the topology are not considered in the mathematical treatment. This simplification is made possible because of the assumption used in this thesis that all flexure elements within flexure systems can be modeled as ideal constraints [37-39], which are infinitely stiff along the directions they constrain while being infinitely compliant in all other directions. Thus, the theory proposed here is well suited to enable an automated approach for rapidly analyzing the mobility and constraint characteristics of compliant mechanisms, structures, and materials that consists of large numbers of flexible elements of various geometries joined together in an interconnected fashion.

CHAPTER 2

Review of Freedom and Constraint Topology

This chapter reviews the freedom and constraint spaces and its underlying mathematics. These spaces will be integral to the new mobility and constraint analysis method introduced later in this thesis.

2.1 Twist and wrench vectors

The instantaneous permissible motions of a general body can be represented as lines (Fig. 2.1) that are mathematically modeled as 6x1 twist vectors, **T**, [9-11] defined as

$$\mathbf{T} = \omega\begin{bmatrix}\mathbf{n} & (\mathbf{c}\times\mathbf{n} + p\mathbf{n})\end{bmatrix}^T, \tag{2.1}$$

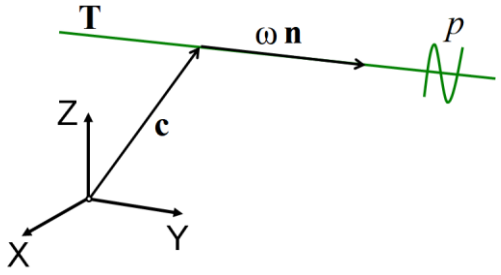

Figure 2.1: Parameters that define a twist vector

where ω is the magnitude of the body's angular velocity about the motion's line, **n** is a 1x3 unit vector that points along the line's axis, **c** is a 1x3 location vector that points from the origin of the coordinate system to any point along that line, and p is the pitch of the motion (i.e., the ratio of how much the

body translates along the line's to how much the body rotates about that axis). If the pitch is zero, the motion is a rotation and its line will be colored red in this paper. If the pitch is non-zero but finite, the motion is a screw and its line will be colored green. If the pitch is infinite, the motion is a translation and its line will be shown as a thick black arrow. Thus, twist vectors used to model translations can be simplified according to

$$\mathbf{T} = v\begin{bmatrix}\mathbf{0} & \mathbf{n}\end{bmatrix}^T, \tag{2.2}$$

where v is the magnitude of the body's linear velocity along the translation's arrow, $\mathbf{0}$ is a 1x3 zero vector, and $\mathbf{n}$ is a 1x3 unit vector that points in the direction of that same arrow.

Constraint loads imposed on a general body can also be represented as lines (Fig. 2.2) that are mathematically modeled as 6x1 wrench vectors, $\mathbf{W}$, [9-11] defined according to Eq. (2.1) except that $\mathbf{T}$ is replaced by $\mathbf{W}$, ω is replaced by f, $\mathbf{c}$ is replaced by $\mathbf{r}$, and p is replaced by q, defined as:

$$\mathbf{W} = f\begin{bmatrix}\mathbf{n} & (\mathbf{r}\times\mathbf{n} + q\mathbf{n})\end{bmatrix}^T \tag{2.3}$$

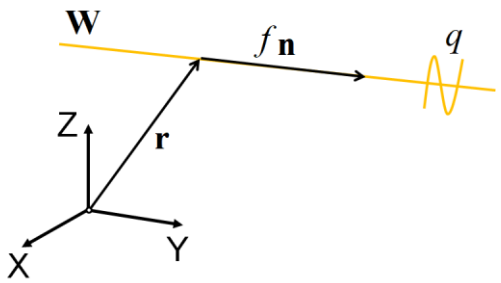

Figure 2.2: Parameters that define a wrench vector

where the scalar value f is the magnitude of the constraining force imposed on the body along the load's line, **r** is a 1x3 location vector that points from the origin of the coordinate system to any point along that line, and q is the ratio of the magnitude of the constraining moment imposed on the body about the line's axis to the magnitude of the constraining force along the same line. If q is zero, the load is a pure force and its line will be colored blue in this paper. If q is non-zero but finite, the motion is a wrench and its line will be colored orange. If q is infinite, the load is a pure moment and its line will be shown as a thick black line with a circular arrow about its axis. Thus, wrench vectors used to model pure moments can be simplified similar to Eq. (2.2):

$$\mathbf{W} = \tau\begin{bmatrix}\mathbf{0} & \mathbf{n}\end{bmatrix}^T \tag{2.4}$$

where τ is the magnitude of the body's pure moment about its line with circular arrows.

2.2 Freedom and constraint spaces

To demonstrate how twist and wrench vectors can be used to model the permissible motions and constraining loads imposed on a body by a flexure element, consider the blade element in Fig. 2.3. This element constrains its body such that it possesses three DOFs shown in the figure—two rotational twist vectors, $\mathbf{T}_1$ and $\mathbf{T}_2$, and one translational twist vector, $\mathbf{T}_3$. The body can also move with every combination of these DOF twist vectors according to

$$\mathbf{T}_{\mathbf{f\ r,e}} = \mathbf{T}_1 + \mathbf{T}_2 + \mathbf{T}_3 = \omega_1 \begin{bmatrix} 1 \\ 0 \\ 0 \\ 0 \\ 0 \\ 0 \end{bmatrix} + \omega_2 \begin{bmatrix} 0 \\ 0 \\ 1 \\ 0 \\ 0 \\ 0 \end{bmatrix} + v_3 \begin{bmatrix} 0 \\ 0 \\ 0 \\ 0 \\ 1 \\ 0 \end{bmatrix} = \begin{bmatrix} \omega_1 \\ 0 \\ \omega_2 \\ 0 \\ v_3 \\ 0 \end{bmatrix} \tag{2.5}$$

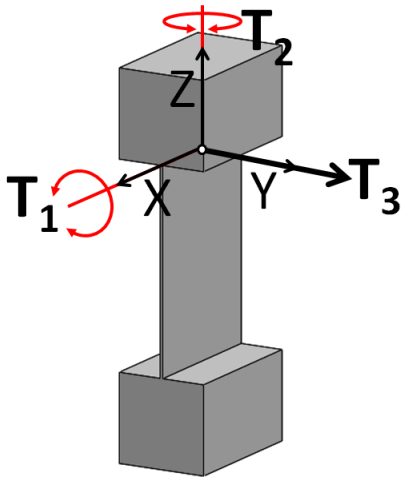

Figure 2.3: DOF of a blade flexure

where $\mathbf{T}_{\mathbf{fre,e}}$ is a twist vector that represents these DOF combinations, ω_1 and ω_2 are the magnitudes of the angular velocities of $\mathbf{T}_1$ and $\mathbf{T}_2$ respectively, and v_3 is the magnitude of the linear velocity of $\mathbf{T}_3$. If all the motion lines that are modeled by $\mathbf{T}_{\mathbf{fre,e}}$ are graphically depicted for all real combinations of ω_1, ω_2, and v_3, the freedom space of the element is produced. A freedom space is a geometric shape, which consists of motion lines, that represents all the ways a body is free to move. The freedom space of the blade element, $\mathbf{T}_{\mathbf{fre,e}}$, is thus a red plane of rotation lines and an orthogonal black translation arrow shown in Fig. 2.4. Thus, a body constrained by a blade element can rotate about any line on the plane of the blade and translate in the direction perpendicular to the blade's plane. Note that the

number of independent twist vectors, *n*, that constitute a freedom space is the number of its DOFs. For a blade element, *n*=3.

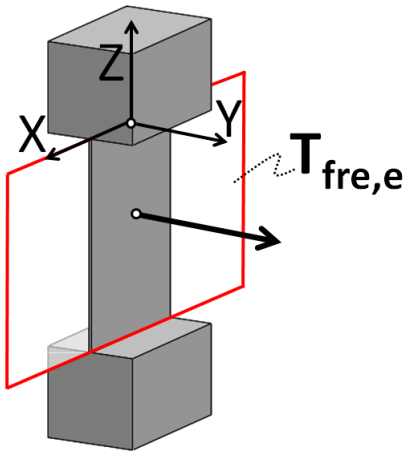

Figure 2.4: Freedom space of a blade flexure

The blade flexure element can also impart three independent constraining loads onto its body as shown in Fig. 2.5—two pure force wrench vectors, $\mathbf{W_1}$ and $\mathbf{W_2}$, and one pure moment wrench vector, $\mathbf{W_3}$. Additionally, the blade element can constrain the body with every combination of these independent wrench vectors in a similar fashion to Eq. (2.5):

$$\mathbf{W_{fre,e}} = \mathbf{W_1} + \mathbf{W_2} + \mathbf{W_3} = f_1\begin{bmatrix}1\\0\\0\\0\\0\\0\end{bmatrix} + f_2\begin{bmatrix}0\\0\\1\\0\\0\\0\end{bmatrix} + \tau_3\begin{bmatrix}0\\0\\0\\0\\1\\0\end{bmatrix} = \begin{bmatrix}f_1\\0\\f_2\\0\\\tau_3\\0\end{bmatrix} \tag{2.6}$$

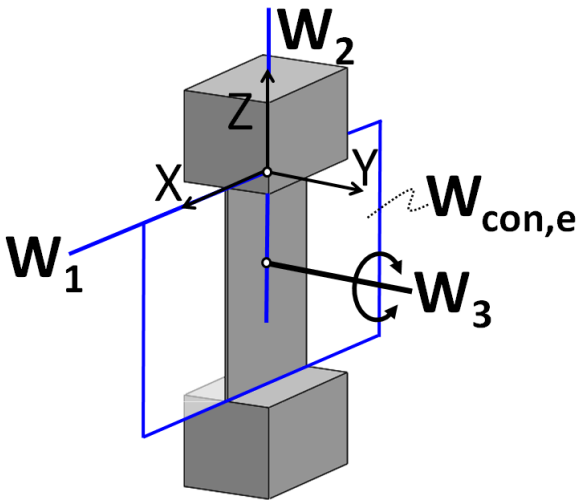

Figure 2.5: Constraint space and constraining actions of a blade flexure

here $\mathbf{T}_{\mathbf{fre,e}}$ is replaced by $\mathbf{W}_{\mathbf{con,e}}$, $\mathbf{T}_1$, $\mathbf{T}_2$, and $\mathbf{T}_3$ are replaced by $\mathbf{W}_1$, $\mathbf{W}_2$, and $\mathbf{W}_3$ respectively, and ω_1, ω_2, and v_3 are replaced by f_1, f_2, and τ_3 respectively. The $\mathbf{W}_{\mathbf{con,e}}$ vector represents all the load combinations that the element can impart onto the body, f_1 and f_2 are the magnitudes of the pure forces of $\mathbf{W}_1$ and $\mathbf{W}_2$ respectively, and τ_3 is the magnitude of the pure moment of $\mathbf{W}_3$. If all the load lines that are modeled by $\mathbf{W}_{\mathbf{con,e}}$ are graphically depicted for all real combinations of f_1, f_2, and τ_3, the constraint space of the element is produced. A constraint space is a geometric shape, which consists of load lines, that represents all the constraining loads imparting on a body that restrict its motions in certain directions. The constraint space of the blade element, $\mathbf{W}_{\mathbf{con,e}}$, is thus a blue plane of force lines and an orthogonal black moment line with a circular arrow about its axis as shown in Fig. 2.5. Thus, a body constrained by a blade element is restricted from moving by all the force lines that lie on the plane of

the blade and by a moment line that is perpendicular to the blade's plane. The blade flexure is one of the special cases where the freedom and constraint space are of the same geometric shape.

Note that the number of independent wrench vectors, *m*, that constitute a constraint space is 6-*n* because of the general relationship [9-11] between freedom spaces, $\mathbf{T_{fre}}$, and their complementary constraint spaces, $\mathbf{W_{con}}$, given by

$$\mathbf{T}_{\mathbf{fre}}^{T}\begin{bmatrix}[0] & [I]\\ [I] & [0]\end{bmatrix}\mathbf{W}_{\mathbf{con}} = 0 \tag{2.7}$$

where [0] is a 3x3 zero matrix and [*I*] is a 3x3 identity matrix.

As another example element, consider the wire flexure shown in Fig. 2.6. This element possesses five DOFs—three orthogonal and intersecting rotational twist vectors, $\mathbf{T_1}$, $\mathbf{T_2}$, and $\mathbf{T_3}$, and two translational twist vectors, $\mathbf{T_4}$ and $\mathbf{T_5}$, that are orthogonal and align with the axes of $\mathbf{T_1}$ and $\mathbf{T_2}$ respectively as shown in the figure. The wire element's freedom space, $\mathbf{T_{fre,e}}$, results from the combination of these five twist vectors as:

$$\mathbf{T}_{\mathbf{fre,e}} = \sum_{i=1}^{n=5}\mathbf{T}_{\mathbf{i}} = \omega_1\begin{bmatrix}1\\0\\0\\0\\0\\0\end{bmatrix} + \omega_2\begin{bmatrix}0\\1\\0\\0\\0\\0\end{bmatrix} + \omega_3\begin{bmatrix}0\\0\\1\\0\\0\\0\end{bmatrix} + v_4\begin{bmatrix}0\\0\\0\\1\\0\\0\end{bmatrix} + v_5\begin{bmatrix}0\\0\\0\\0\\1\\0\end{bmatrix} = \begin{bmatrix}\omega_1\\ \omega_2\\ \omega_3\\ v_4\\ v_5\\ 0\end{bmatrix} \tag{2.8}$$

where ω_1, ω_2, and ω_3 are the magnitudes of the angular velocities of $\mathbf{T_1}$, $\mathbf{T_2}$, and $\mathbf{T_3}$ respectively, and v_4 and v_5 are the magnitudes of the linear velocities of $\mathbf{T_4}$ and $\mathbf{T_5}$. The element's freedom space is

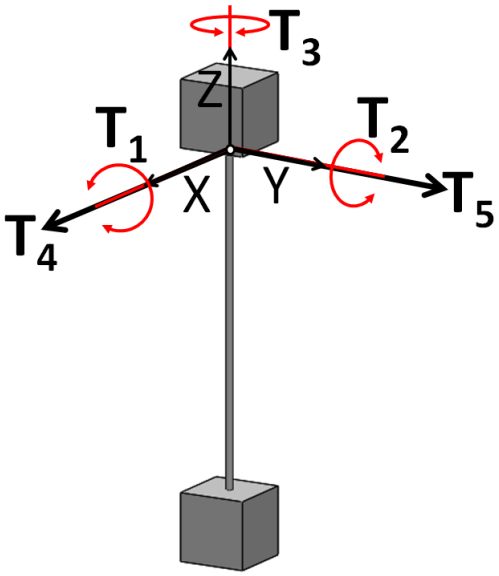

Figure 2.6: DOF of a wire flexure

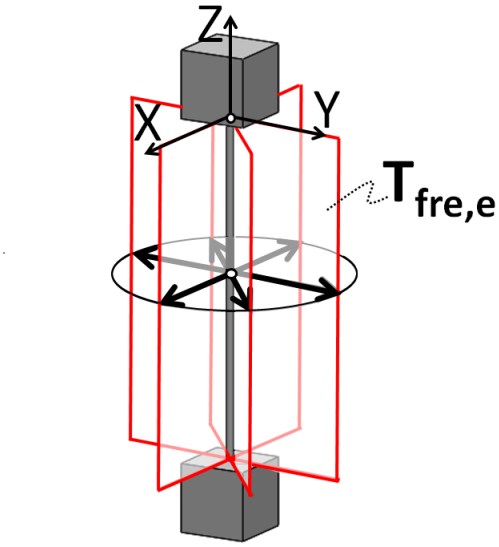

Figure 2.7: Freedom space of a wire flexure

graphically depicted in Fig. 2.7 as *(i)* red planes of rotation lines that intersect along the wire's axis, *(ii)* a black disk of translation arrows that point in directions that are perpendicular to the wire's axis, and *(iii)* green screw lines that are described in Hopkins [37,38] but not shown in the figure to avoid visual clutter. The element's complementary constraint space, $\mathbf{W}_{\mathbf{con,e}}$, can be calculated using Eqs. (2.7) and (2.8) and consists of the single blue line shown in Fig. 2.8 modeled by

$$\mathbf{W}_{\mathbf{con,e}} = \mathbf{W}_{\mathbf{1}} = f_1\begin{bmatrix}0 & 0 & 1 & 0 & 0 & 0\end{bmatrix}^T \tag{2.9}$$

where f_1 is the magnitude of the constraining force wrench vector, $\mathbf{W}_{\mathbf{1}}$, imparted by the wire element along its axis to the body in Fig. 2.8.

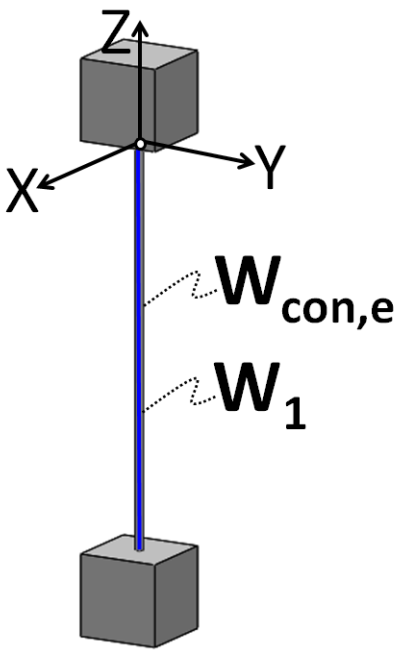

Figure 2.8: Constraint space of a wire flexure

Mobility analysis of a flexure system is successfully achieved when the freedom space of the system's stage is identified (i.e., when one knows all the ways the system's stage is free to move). Synthesis of a flexure system is successfully achieved when the constraint space of every element in the flexure system is specified (i.e., when one specifies all the constraining action every flexure element provide). Even though there are infinite linear combinations of twist and wrench vectors, there are only a finite number of geometric shapes and thus freedom and constraint spaces they manifests. The comprehensive chart by Hopkins [38] previously given in Fig. 1.3 contains all possible freedom and constraint spaces, and is essential to the rest of this work. The FACT method is used to interpret between the physical implementation of flexure elements and the mathematical expression of twist and wrench vectors.

2.3 Parallel and serial flexure systems

Current analysis and synthesis approach with freedom and constraint topology hinges on two primary principles:

(1) Parallel Configurations: A system's constraint space can be found by linearly combining the constraint spaces of its constituent flexure elements and/or systems when they are arranged in parallel. A system's freedom space can be found by identifying the intersection of the freedom spaces of its constituent flexure elements and/or systems when they are arranged in parallel.

(2) Serial Configuration: A system's freedom space can be found by linearly combining the freedom spaces of its stacked flexure subsystems when they are arranged in series. A system's constraint space can be found by identifying the intersection of the constraint spaces of its stacked flexure subsystems when they are arranged in series.

To demonstrate principle ***(1)***, consider the parallel system shown in Fig. 2.9 that consists of a blade element, *e1*, arranged in parallel with a wire element, *e2*. The constraint space of element *e1* is the blue plane from Fig. 2.5. Given the coordinate system shown in Fig. 2.10, this constraint space, $\mathbf{W}_{\mathbf{con,e1}}$, can be expressed as

$$\mathbf{W}_{\mathbf{con,e1}} = \sum_{j=1}^{m=3} \mathbf{W}_{\mathbf{j}} = f_1 \begin{bmatrix} 1 \\ 0 \\ 0 \\ 0 \\ 0 \\ D/2 \end{bmatrix} + f_2 \begin{bmatrix} 0 \\ 0 \\ 1 \\ -D/2 \\ 0 \\ 0 \end{bmatrix} + \tau_3 \begin{bmatrix} 0 \\ 0 \\ 0 \\ 0 \\ 1 \\ 0 \end{bmatrix} = \begin{bmatrix} f_1 \\ 0 \\ f_2 \\ -f_2 D/2 \\ \tau_3 \\ f_1 D/2 \end{bmatrix} \tag{2.10}$$

where f_1 and f_2 are the force magnitudes of $\mathbf{W_1}$ and $\mathbf{W_2}$ in Fig. 2.10 respectively, τ_3 is the moment magnitude of $\mathbf{W_3}$, and D is a scalar distance labeled in the same figure. The constraint space of element *e2* is the blue line from Fig. 2.8. Given the coordinate system in Fig. 2.10, this constraint space, $\mathbf{W}_{\mathbf{con,e2}}$, can be expressed as

$$\mathbf{W}_{\mathbf{con,e2}} = \mathbf{W_4} = f_4 \begin{bmatrix} 0 & 0 & 1 & (D/2) & 0 & 0 \end{bmatrix}^T \tag{2.11}$$

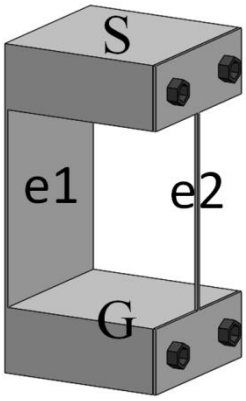

Figure 2.9: A parallel flexure system

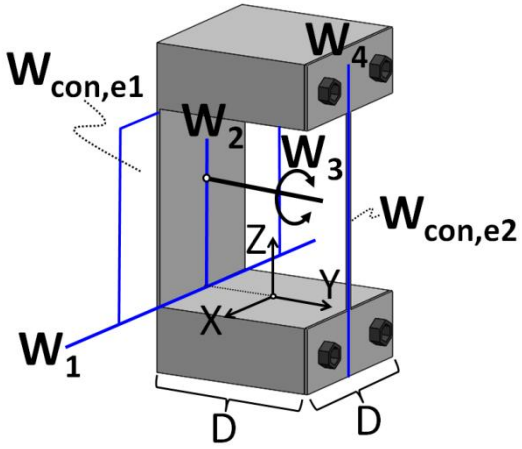

Figure 2.10: Constraint space of individual flexure elements within a parallel flexure system

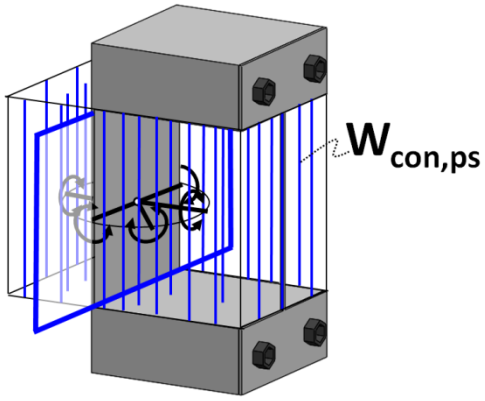

Figure 2.11: Constraint space of a parallel flexure system

where f_4 is the force magnitude of $\mathbf{W_4}$ in Fig. 2.10. Thus, according to principle ***(1)***, since elements *e1* and *e2* are arranged in parallel, the constraint space of the parallel system, $\mathbf{W_{con,ps}}$, could be calculated by linearly combining Eq. (2.10) with Eq. (2.11) (i.e., $\mathbf{W_{con,ps}}=\mathbf{W_{con,e1}}+\mathbf{W_{con,e2}}$), and thereby describing all the constraining actions exerted on the stage by both flexure elements. The resulting parallel system's constraint space is shown in Fig. 2.11. This space consists of *(i)* a plane of blue force lines that is coplanar with the system's blade element, *(ii)* a box of parallel blue force lines that are parallel with the axis of the system's wire element, *(iii)* a disk of black pure moment lines that point in directions perpendicular to the wire's axis, and *(iv)* orange wrench lines that are described in Hopkins [37,38] but are not shown in Fig. 2.11 to avoid visual clutter.

The parallel system's freedom space, $\mathbf{T_{fre,ps}}$, can be calculated using $\mathbf{W_{con,ps}}$ in Eq. (2.7). This space, shown in Fig. 2.12, consists of *(i)* a plane of parallel red rotation lines that are parallel to the axis of the wire element but are coplanar with the plane of the blade element, and *(ii)* a black translation arrow that is perpendicular to the same plane. This freedom space, $\mathbf{T_{fre,ps}}$, results from the linear combination of two independent twist vectors (e.g., $\mathbf{T_1}$ and $\mathbf{T_2}$ in Fig. 2.12) according to

$$\mathbf{T_{fre,ps}} = \sum_{i=1}^{n=2} \mathbf{T_i} = \omega_1 \begin{bmatrix} 0 \\ 0 \\ 1 \\ -D/2 \\ 0 \\ 0 \end{bmatrix} + v_2 \begin{bmatrix} 0 \\ 0 \\ 0 \\ 0 \\ 1 \\ 0 \end{bmatrix} = \begin{bmatrix} 0 \\ 0 \\ \omega_1 \\ -\omega_1 D/2 \\ v_2 \\ 0 \end{bmatrix} \tag{2.12}$$

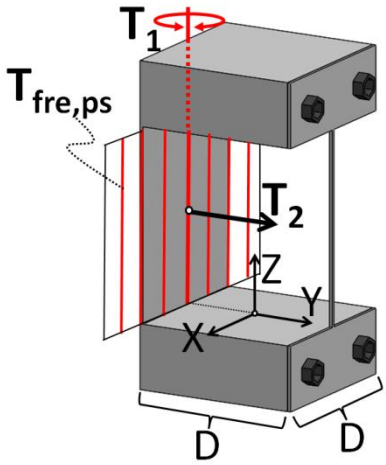

Figure 2.12: Freedom space of a parallel flexure system

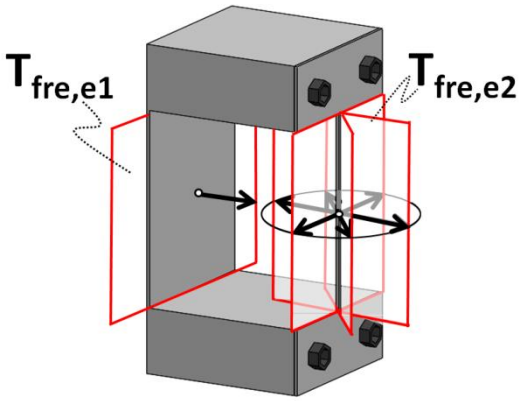

Figure 2.13: Freedom space of individual flexure elements within a parallel flexure system

where ω_1 is the magnitude of the angular velocity of $\mathbf{T_1}$ in Fig. 2.12, and v_2 is the magnitude of the linear velocity of $\mathbf{T_2}$ in the same figure. Note that in accordance with principle ***(1)***, the parallel system's freedom space (Fig. 2.12) is the intersection of the freedom spaces of the system's

constituent elements (i.e., $\mathbf{T_{fre,e1}}$ and $\mathbf{T_{fre,e2}}$ shown in Fig. 2.13). In other words, the motion lines that constitute the space of Fig. 2.13 are the same motion lines that are commonly shared between the two spaces shown in Fig. 2.13, and thereby represent the motion allowed by both of the flexure elements within the system. Recall that the freedom space of a blade element was given in Fig. 2.4 and the freedom space of a wire element was given in Fig. 2.7.

The constraint space of Fig. 2.11 and the freedom space in Fig. 2.12 can be found in the FACT library of Fig. 1.3, falling under category of the 2nd item in the 2 DOF column. Be careful to notice that the freedom and constraint space drawn in Fig. 1.3 is oriented in a different direction.

To demonstrate principle ***(2)***, consider the serial system shown in Fig. 2.14 that consists of two stacked parallel subsystems, *ps1* and *ps2*, of the kind shown in Fig. 2.9. The freedom spaces of each subsystem (Fig. 2.12) are shown superimposed on the serial system in Fig. 2.14. Given the coordinate system shown in Fig. 2.15, the freedom space of *ps1*, $\mathbf{T_{fre,ps1}}$, can be expressed as

$$\mathbf{T_{fre,ps1}} = \mathbf{T_1} + \mathbf{T_2} = \omega_1 \begin{bmatrix} 0 \\ 0 \\ 1 \\ 0 \\ 0 \\ 0 \end{bmatrix} + v_2 \begin{bmatrix} 0 \\ 0 \\ 0 \\ 0 \\ 1 \\ 0 \end{bmatrix} = \begin{bmatrix} 0 \\ 0 \\ \omega_1 \\ 0 \\ v_2 \\ 0 \end{bmatrix} \tag{2.13}$$

where ω_1 is the angular velocity magnitude of $\mathbf{T_1}$, and v_2 is the linear velocity magnitude of $\mathbf{T_2}$ in Fig. 2.15. Given the coordinate system of Fig. 2.15, the freedom space of *ps2*, $\mathbf{T_{fre,ps2}}$, can be expressed as

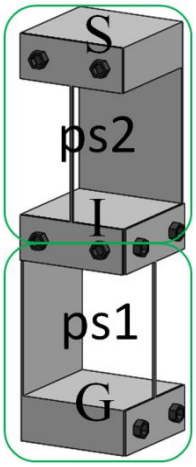

Figure 2.14: A serial flexure system

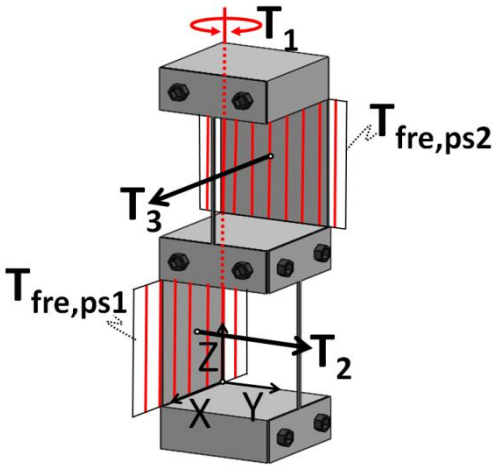

Figure 2.15: Freedom space of the flexure subsystems within serial flexure system

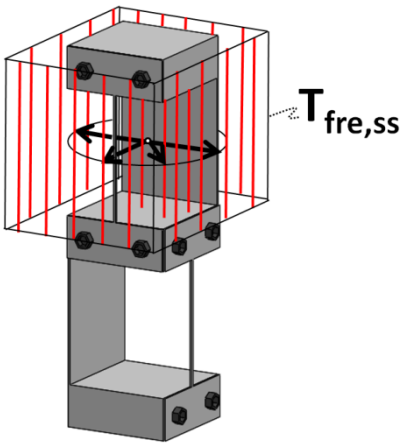

Figure 2.16: Freedom space of the stage of the serial flexure system

$$\mathbf{T_{fre,ps2}} = \mathbf{T_1} + \mathbf{T_3} = \omega_1 \begin{bmatrix} 0 \\ 0 \\ 1 \\ 0 \\ 0 \\ 0 \end{bmatrix} + v_3 \begin{bmatrix} 0 \\ 0 \\ 0 \\ 1 \\ 0 \\ 0 \end{bmatrix} = \begin{bmatrix} 0 \\ 0 \\ \omega_1 \\ v_3 \\ 0 \\ 0 \end{bmatrix} \tag{2.14}$$

where ω_1 is the angular velocity magnitude of $\mathbf{T_1}$, and v_3 is the linear velocity magnitude of $\mathbf{T_3}$ in Fig. 2.15. Thus, according to principle ***(2)***, since the parallel subsystems *ps1* and *ps2* are arranged in series, the freedom space of the serial system, $\mathbf{T_{fre,ss}}$, could be calculated by linearly combining Eq. (2.13) with Eq. (2.14) (i.e., $\mathbf{T_{fre,ss}}=\mathbf{T_{fre,ps1}}+\mathbf{T_{fre,ps2}}$). The resulting serial system's freedom space, shown in Fig. 2.16, consists of *(i)* a box of parallel red rotation lines that are parallel with the axes of the system's wire elements, and *(ii)* a disk of black translation arrows that point in directions that are perpendicular to these axes.

The serial system's constraint space, $\mathbf{W_{con,ss}}$, can be calculated using $\mathbf{T_{fre,ss}}$ in Eq. (2.7). This space, shown in Fig. 2.17, consists of *(i)* a box of parallel blue force lines that are parallel with the axes of the system's wire elements, and *(ii)* a disk of black moment lines that point in directions that are perpendicular to these axes. This constraint space, $\mathbf{W_{con,ss}}$, results from the linear combination of three independent wrench vectors (e.g., $\mathbf{W_1}$, $\mathbf{W_2}$, and $\mathbf{W_3}$ in Fig. 2.17) according to

$$\mathbf{W}_{\mathbf{con,ss}} = \sum_{j=1}^{m=3} \mathbf{W}_{\mathbf{j}} = f_1 \begin{bmatrix} 0 \\ 0 \\ 1 \\ 0 \\ 0 \\ 0 \end{bmatrix} + \tau_2 \begin{bmatrix} 0 \\ 0 \\ 0 \\ 0 \\ 1 \\ 0 \end{bmatrix} + \tau_3 \begin{bmatrix} 0 \\ 0 \\ 0 \\ 1 \\ 0 \\ 0 \end{bmatrix} = \begin{bmatrix} 0_1 \\ 0 \\ f_1 \\ \tau_3 \\ \tau_2 \\ 0 \end{bmatrix} \tag{2.15}$$

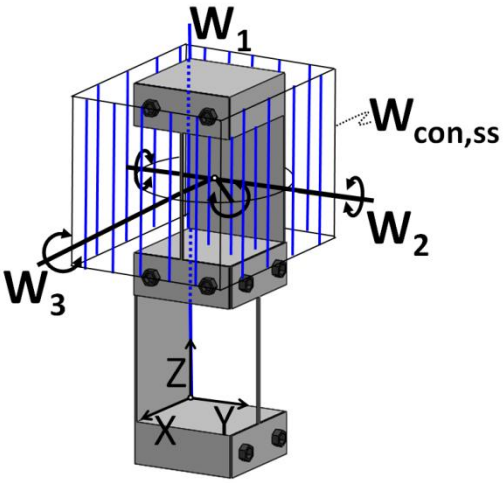

Figure 2.17: Constraint space of the stage of the serial flexure system

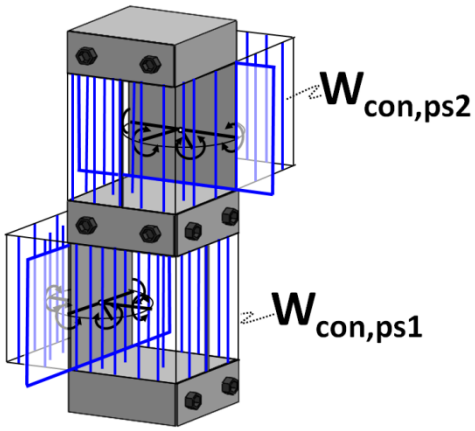

Figure 2.18: Constraint space of the flexure subsystems within serial flexure system

where f_1 is the force magnitude of $\mathbf{W_1}$ in Fig. 2.17, and τ_2 and τ_3 are the moment magnitudes of $\mathbf{W_2}$ and $\mathbf{W_3}$ in the same figure. Note that in accordance with principle ***(2)***, the serial system's constraint space (Fig. 2.17) is the intersection of the constraint spaces of the system's stacked parallel subsystems (i.e., $\mathbf{W_{con,ps1}}$ and $\mathbf{W_{con,ps2}}$ shown in Fig. 2.18). In other words, the load lines that constitute the space of Fig. 2.17 are the same load lines that are commonly shared between the two spaces shown in Fig. 2.18. Recall that the constraint space of each parallel subsystem was given in Fig. 2.11.

2.4 Non-interconnected hybrid flexure systems

Since principles ***(1)*** and ***(2)*** pertain to flexure elements and/or subsystem's arranged in parallel or series, these principles can only be used to perform the mobility analysis of flexure systems that can be broken into parallel and serial subsystems. Consider the hybrid system in Fig. 2.19 that consists of two serial subsystems (i.e., limbs) arranged in parallel. Once the constraint spaces of each parallel subsystem, *ps1* through *ps4*, have been identified according to the principles reviewed in this section, the freedom space of the system's stage can be determined using an operator, *Z*. This operator utilizes Eq. (2.7) to determine the complementary freedom space of a constraint space and vice versa (i.e., $Z(\mathbf{W_{con}})=\mathbf{T_{fre}}$ and $Z(\mathbf{T_{fre}})=\mathbf{W_{con}}$). Thus, if $\mathbf{W_{con,ps1}}$, $\mathbf{W_{con,ps2}}$, $\mathbf{W_{con,ps3}}$, and $\mathbf{W_{con,ps4}}$, are the constraint spaces of the parallel subsystems, *ps1* through *ps4*, in Fig. 2.19 respectively, the hybrid system's freedom space, $\mathbf{T_{fre,hs}}$, (i.e., the freedom space of the system's stage) can be calculated according to

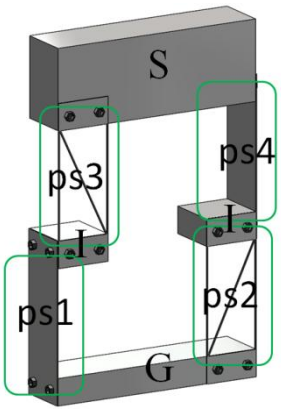

Figure 2.19: A hybrid flexure system

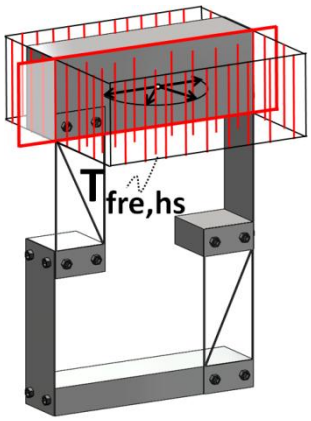

Figure 2.20: Freedom space of a hybrid flexure system

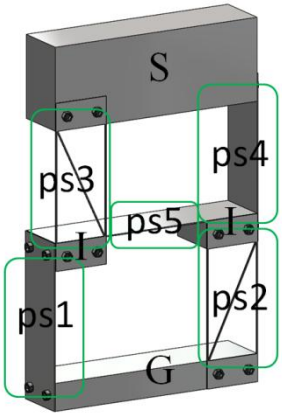

Figure 2.21: An interconnected hybrid flexure system

$$\mathbf{T}_{\mathbf{fre,hs}} = Z\left(Z\left(Z(\mathbf{W}_{\mathbf{con,ps1}}) + Z(\mathbf{W}_{\mathbf{con,ps3}})\right) + Z\left(Z(\mathbf{W}_{\mathbf{con,ps2}}) + Z(\mathbf{W}_{\mathbf{con,ps4}})\right)\right) \tag{2.16}$$

This freedom space, shown in Fig. 2.20, consists of *(i)* a plane of red rotation lines that is coplanar with the front face of the system's stage, *(ii)* a box of parallel red rotation lines that are directed vertically, *(iii)* a disk of black translation arrows that point in directions perpendicular to these parallel rotation lines, and *(iv)* green screw lines that are described in Hopkins [37,38] but are not shown in Fig. 2.20 to avoid visual clutter. If, however, the intermediate bodies of the example system are joined together by another parallel subsystem, *ps5*, as shown in Fig. 2.21, principles ***(1)*** and ***(2)*** cannot be applied to the system's mobility analysis because the system can't be broken into parallel and serial subsystems. Thus, the system of Fig. 2.21 is an interconnected hybrid system, which requires new theory to analyze (i.e., determine its stage's freedom space).

One of the primary objectives of this thesis is to introduce a systematic approach for successfully navigating the freedom and constraint spaces of a system's constituent elements and subsystems such that the mobility analysis and topological synthesis of a general flexure system can be achieved. The other primary objective of this thesis is to introduce a systematic approach for successfully navigating these freedom and constraint spaces such that designers can identify the system's constraint characteristics (i.e., perform constraint analysis) and specify desired designs accordingly.

CHAPTER 3

Mobility Analysis of Flexure Systems with Screw Algebra and Graph Theory

This chapter introduces two new complementary screw-algebra and graph-theory approaches for systematically performing the mobility analysis of flexure systems of any configuration and complexity—including and especially interconnected hybrid flexure systems. Although similar to prior approaches [27,28], the first approach focuses on the mobility analysis of compliant mechanisms (i.e., flexure systems) instead of rigid mechanisms. It can also be used to identify whether a system is under-constrained or not. The second approach is complementary to the first approach (i.e., it uses complementary constraint spaces instead of freedom spaces) but it can be used to identify if a system is over-constrained or exactly-constrained (i.e., it is used to perform constraint analysis). The interconnected hybrid system of Fig. 2.21 will be analyzed as a case study for the theory of this section.

3.1 Freedom-space-based Approach to Mobility Analysis

This section introduces a freedom-space-based approach for calculating the freedom space of a general flexure system's stage (i.e., for performing mobility analysis). To determine the freedom space of a flexure system's stage using this approach, it is first necessary to identify the freedom spaces of each set of flexure elements that join the system's rigid bodies together. Such sets of flexure elements are analogous to the joints of traditional rigid mechanisms (e.g., revolute or prism joints) that guide

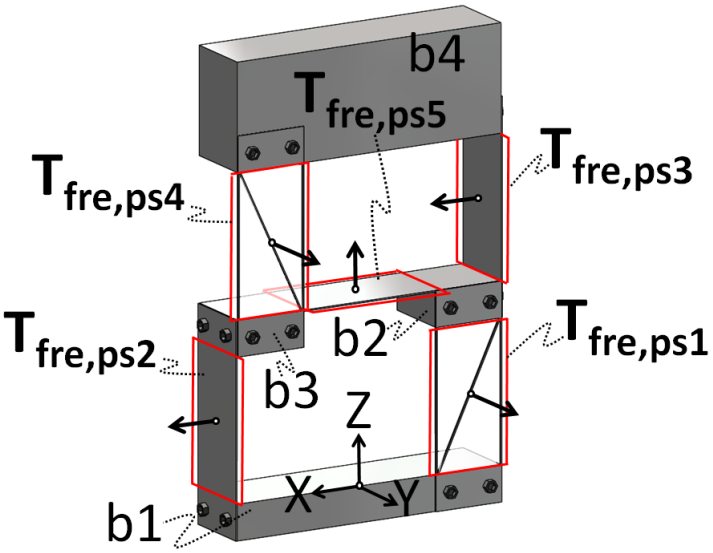

Figure 3.1: Freedom spaces of each parallel subsystem within the system

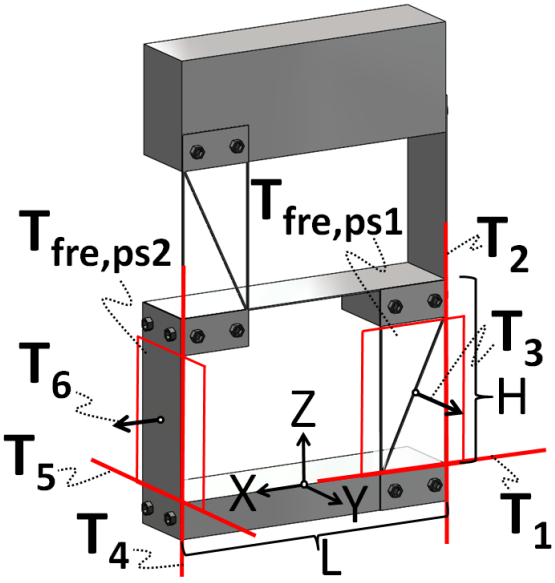

Figure 3.2: Twist vectors within freedom spaces

the motions of their rigid links and join them together. Thus, the 'compliant joints' of the interconnected hybrid flexure system of Fig. 2.21 are the five parallel subsystems labeled *ps1* through *ps5* in the figure. Their respective freedom spaces, $\mathbf{T}_{\mathbf{fre,ps1}}$ through $\mathbf{T}_{\mathbf{fre,ps5}}$, can each be identified using the theory of chapter 2. For the example of Fig. 2.21, these freedom spaces are shown in Fig. 3.1. They are the blade flexure's freedom space from Fig. 2.4 and thus consist of a red plane of rotation lines and a black translation arrow that is perpendicular to that plane.

Once the freedom spaces of the system's compliant joints have been identified, each freedom space must be mathematically modeled. A freedom space can be modeled mathematically according to the theory provided in chapter 2 by selecting *n* independent twist vectors from within the freedom space and linearly combining them. Recall that *n* is the number of DOFs or independent twist vectors that constitute a freedom space. For the example system of Fig. 3.1, the freedom spaces of the compliant joints each possess three independent twist vectors within their geometry (i.e., *n*=3). Thus the freedom space, $\mathbf{T}_{\mathbf{fre,ps1}}$, of the parallel subsystem *ps1* joint could be mathematically modeled by the following linear combination

$$\mathbf{T}_{\mathbf{fre,ps1}} = \sum_{i=1}^{n=3} \mathbf{T}_{\mathbf{i}} = \omega_1 \begin{bmatrix} 1 \\ 0 \\ 0 \\ 0 \\ 0 \\ 0 \end{bmatrix} + \omega_2 \begin{bmatrix} 0 \\ 0 \\ 1 \\ 0 \\ L/2 \\ 0 \end{bmatrix} + v_3 \begin{bmatrix} 0 \\ 0 \\ 0 \\ 0 \\ 1 \\ 0 \end{bmatrix} = [jft]_{ps1} \mathbf{x}_{\mathbf{ps1}} \tag{3.1}$$

where $\mathbf{T_1}$, $\mathbf{T_2}$, and $\mathbf{T_3}$, are the independent twist vectors shown and defined according to the global coordinate system in Fig. 3.2, ω_1, ω_2 , and v_3 are the velocity magnitudes of these twist vectors respectively, L is the length defined in the same figure, $[jft]_{ps1}$ is the joint-freedom-topology matrix of the parallel subsystem *ps1* defined according to

$$[jft]_{ps1} = \begin{bmatrix} 1 & 0 & 0 & 0 & 0 & 0 \\ 0 & 0 & 1 & 0 & L/2 & 0 \\ 0 & 0 & 0 & 0 & 1 & 0 \end{bmatrix}^T, \tag{3.2}$$

and $\mathbf{x_{ps1}}$ is the velocity magnitude vector of *ps1* defined as

$$\mathbf{x_{ps1}} = [\omega_1 \quad \omega_2 \quad v_3]^T. \tag{3.3}$$

Note that $\mathbf{T_1}$, $\mathbf{T_2}$, and $\mathbf{T_3}$ in Fig. 3.2 are not the only set of independent twist vectors that could have been selected to model $\mathbf{T_{fre,ps1}}$. Any arbitrary set of three independent twist vectors that lie within the *ps1* freedom space could have be selected as the basis of the space.

The freedom space, $\mathbf{T_{fre,ps2}}$, of the parallel subsystem *ps2* could also be modeled using the $\mathbf{T_4}$, $\mathbf{T_5}$, and $\mathbf{T_6}$ independent twist vectors in Fig. 3.2 to construct the corresponding $[jft]_{ps2}$ matrix according to

$$[jft]_{ps2} = \begin{bmatrix} 0 & 0 & 1 & 0 & -L/2 & 0 \\ 0 & 1 & 0 & 0 & 0 & L/2 \\ 0 & 0 & 0 & 1 & 0 & 0 \end{bmatrix}^T \tag{3.4}$$

and the corresponding velocity magnitude vector, $\mathbf{x_{ps2}}$, according to

$$\mathbf{x_{ps2}} = [\omega_4 \quad \omega_5 \quad v_6]^T \tag{3.5}$$

where ω_4, ω_5, and v_6 are the velocity magnitudes of $\mathbf{T_4}$, $\mathbf{T_5}$, and $\mathbf{T_6}$ in Fig. 3.2 respectively.

Once all the system's compliant-joint freedom spaces, $\mathbf{T_{fre,ps1}}$ through $\mathbf{T_{fre,ps5}}$, have been modeled by constructing their corresponding joint-freedom-topology matrices, $[jft]_{ps1}$ through $[jft]_{ps5}$, and their corresponding velocity magnitude vectors, $\mathbf{x_{ps1}}$ through $\mathbf{x_{ps5}}$, the system's rigid bodies should be labeled with numbers. In Fig. 3.1, the system's ground is labeled *b1*, the stage is labeled *b4*, and the intermediate bodies are labeled *b2* and *b3*. A graph can be constructed that details what rigid bodies, shown as point nodes or vertices in Fig. 3.3, are connected by what compliant-joint freedom spaces, shown as edges or arrows in the same figure. The direction of these arrows can be arbitrarily defined at the beginning of the analysis process, but it is important to recognize that the way they are defined establishes an important convention that must be adhered to throughout the remainder of the analysis process to produce correct results.

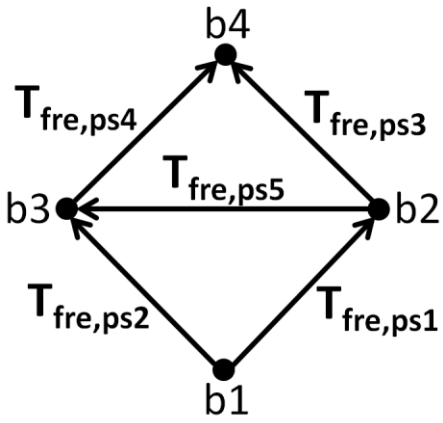

Figure 3.3: Graphical representation of a system with edges as freedom spaces

Although interconnected hybrid flexure systems cannot be decomposed into purely serial or parallel subsystems and consequently cannot be treated using principles ***(1)*** and ***(2)*** from chapter 2, different serial paths can be identified that join the system's ground to its stage. In the example of Fig. 3.3, for instance, four unique serial paths exist that can be drawn from the system's ground to its stage. These serial paths can each be expressed as linear combinations of their parallel-subsystem freedom spaces (i.e., $\mathbf{T_{fre,ps1}+T_{fre,ps3}}$, $\mathbf{T_{fre,ps2}+T_{fre,ps4}}$, $\mathbf{T_{fre,ps1}+T_{fre,ps5}+T_{fre,ps4}}$, $\mathbf{T_{fre,ps2}-T_{fre,ps5}+T_{fre,ps3}}$). Note that the freedom space's sign is positive if the path moves from the specified arrow's tail to its head, but is negative if the path moves from the arrow's head to its tail. The permissible motions of the system's stage (i.e., the stage's freedom space) can be calculated by equating different combinations of these freedom-space paths according to

$$
\begin{aligned}
\mathbf{T}_{\mathbf{fre,ps1}} + \mathbf{T}_{\mathbf{fre,ps3}} &= \mathbf{T}_{\mathbf{fre,ps1}} + \mathbf{T}_{\mathbf{fre,ps5}} + \mathbf{T}_{\mathbf{fre,ps4}} \\
\mathbf{T}_{\mathbf{fre,ps1}} + \mathbf{T}_{\mathbf{fre,ps3}} &= \mathbf{T}_{\mathbf{fre,ps2}} + \mathbf{T}_{\mathbf{fre,ps4}} \\
\mathbf{T}_{\mathbf{fre,ps1}} + \mathbf{T}_{\mathbf{fre,ps3}} &= \mathbf{T}_{\mathbf{fre,ps2}} - \mathbf{T}_{\mathbf{fre,ps5}} + \mathbf{T}_{\mathbf{fre,ps3}} \\
\mathbf{T}_{\mathbf{fre,ps1}} + \mathbf{T}_{\mathbf{fre,ps5}} + \mathbf{T}_{\mathbf{fre,ps4}} &= \mathbf{T}_{\mathbf{fre,ps2}} + \mathbf{T}_{\mathbf{fre,ps4}} \\
\mathbf{T}_{\mathbf{fre,ps1}} + \mathbf{T}_{\mathbf{fre,ps5}} + \mathbf{T}_{\mathbf{fre,ps4}} &= \mathbf{T}_{\mathbf{fre,ps2}} - \mathbf{T}_{\mathbf{fre,ps5}} + \mathbf{T}_{\mathbf{fre,ps3}} \\
\mathbf{T}_{\mathbf{fre,ps2}} + \mathbf{T}_{\mathbf{fre,ps4}} &= \mathbf{T}_{\mathbf{fre,ps2}} - \mathbf{T}_{\mathbf{fre,ps5}} + \mathbf{T}_{\mathbf{fre,ps3}}
\end{aligned}
\tag{3.6}
$$

By equating the different path combinations in Eq. (3.6), the velocity magnitudes that correspond with the twist vectors that are commonly shared by the freedom-space paths are preserved, while the magnitudes that correspond with the twist vectors that are not shared are forced to be zero to make the equation true. Note, therefore, that while a linear combination of vector spaces is determined by summing the spaces together, an intersection of vector spaces is determined by equating the spaces. By subtracting the right side of Eq. (3.6) from its left side and by expressing the parallel-subsystem freedom spaces in the form given in Eq. (3.1), the following matrix-based equation is produced

$$
\begin{bmatrix}
[0] & [0] & [jft]_{ps3} & -[jft]_{ps4} & -[jft]_{ps5} \\
[jft]_{ps1} & -[jft]_{ps2} & [jft]_{ps3} & -[jft]_{ps4} & [0] \\
[jft]_{ps1} & -[jft]_{ps2} & [0] & [0] & [jft]_{ps5} \\
[jft]_{ps1} & -[jft]_{ps2} & [0] & [0] & [jft]_{ps5} \\
[jft]_{ps1} & -[jft]_{ps2} & -[jft]_{ps3} & [jft]_{ps4} & 2[jft]_{ps5} \\
[0] & [0] & -[jft]_{ps3} & [jft]_{ps4} & [jft]_{ps5}
\end{bmatrix}
\begin{bmatrix}
\mathbf{x}_{\mathbf{ps1}} \\
\mathbf{x}_{\mathbf{ps2}} \\
\mathbf{x}_{\mathbf{ps3}} \\
\mathbf{x}_{\mathbf{4ps}} \\
\mathbf{x}_{\mathbf{ps5}}
\end{bmatrix}
= \mathbf{0}
\tag{3.7}
$$

where [0] is a 6x6 matrix of zeros, $[jft]_{ps1}$ through $[jft]_{ps5}$ are the system's joint-freedom-topology matrices that correspond with the freedom spaces of each compliant joint labeled $\mathbf{T}_{\mathbf{fre,ps1}}$ through

$\mathbf{T}_{\mathbf{fre,ps5}}$ in Fig. 3.1, $\mathbf{x}_{\mathbf{ps1}}$ through $\mathbf{x}_{\mathbf{ps5}}$ are the velocity magnitude vectors that correspond with the same freedom spaces, and **0** is a vector of zeros.

Note that the velocity magnitudes that satisfy the combination of equations in Eq. (3.6) result from the null space of the matrix consisting of the system's joint-freedom-topology matrices in Eq. (3.7). The significance of these velocity magnitudes toward finalizing the system's mobility analysis will be discussed later in this section. For now, it is sufficient to note that each row in Eqs. (3.6) and (3.7) corresponds with a unique closed-loop path that links the system's ground to its stage (i.e., the linear combinations on the left side of Eq. (3.6)) and then back to its ground (i.e., the negative values of the linear combinations on the right side of Eq. (3.6)). Thus, the matrix in Eq. (3.7) represents six unique closed-loop paths throughout the interconnected system. It is important here to emphasize, however, that not all of these closed-loop paths are necessary to calculate the system's desired velocity magnitude vectors.

Graph theory provides a means for rapidly determining the fewest number of necessary closed-loop paths within a general flexure system to construct the smallest matrix possible for most efficiently calculating the system's desired velocity magnitude vectors. To this end, the incidence matrix [12,13], [*C*], can be constructed using the schematic graph of any flexure system of interest, similar to the one diagrammed in Fig. 3.3 for the system of this section's example. A general incidence matrix possesses as many rows as there are edges or arrows in the graph being analyzed and as many columns as there are vertices or nodes in the same graph. The component in row *e* and

column *u* of the matrix will be 1 if the edge's arrow that corresponds with the freedom space labeled *e* (i.e., $\mathbf{T}_{\mathbf{fre,pse}}$), points into the node or vertex labeled *u* (i.e., *bu*). This component will be -1 if the edge's arrow points out of the vertex and will be 0 if the edge's arrow doesn't point into or out of the vertex. The incidence matrix of the system of Fig. 3.3 is

$$[C]=\begin{bmatrix} -1 & 1 & 0 & 0 \\ -1 & 0 & 1 & 0 \\ 0 & -1 & 0 & 1 \\ 0 & 0 & -1 & 1 \\ 0 & -1 & 1 & 0 \end{bmatrix} \tag{3.8}$$

According to graph theory [12,13], the left null space of the incidence matrix produces a matrix, [*Q*], that contains information pertaining to the fewest number of independent closed-loop paths within the graph according to

$$[C]^T[Q]=[0] \tag{3.9}$$

The [*Q*] matrix of the system of Fig. 3.3 can, thus be calculated using Eq. (3.8) in Eq. (3.9) according to

$$[Q]=\begin{bmatrix} -1 & 1 & -1 & 1 & 0 \\ 1 & -1 & 0 & 0 & 1 \end{bmatrix}^T. \tag{3.10}$$

If the system's joint-freedom-topology matrices, $[jft]_{ps1}$ through $[jft]_{ps5}$, are then inserted inside their respective columns within the transpose of the $[Q]$ matrix from Eq. (3.10) and the resulting matrix is multiplied by the velocity magnitude vectors according to

$$\begin{bmatrix} -[jft]_{ps1} & [jft]_{ps2} & -[jft]_{ps3} & [jft]_{ps4} & [0] \\ [jft]_{ps1} & -[jft]_{ps2} & [0] & [0] & [jft]_{ps5} \end{bmatrix} \begin{bmatrix} \mathbf{x}_{ps1} \\ \mathbf{x}_{ps2} \\ \mathbf{x}_{ps3} \\ \mathbf{x}_{ps4} \\ \mathbf{x}_{ps5} \end{bmatrix} = [FT]\mathbf{X} = \mathbf{0} \tag{3.11}$$

Eq. (3.7) is simplified from six closed-loop paths to two independent closed-loop paths. The first of these paths, which corresponds with the top row of Eq. (3.11), is shown as a series of green dotted arrows in Fig. 3.4. The second of these paths, which corresponds with the bottom row of Eq. (3.11), is shown as a series of dashed purple arrows in the same figure. Note that the signs of the joint-freedom-

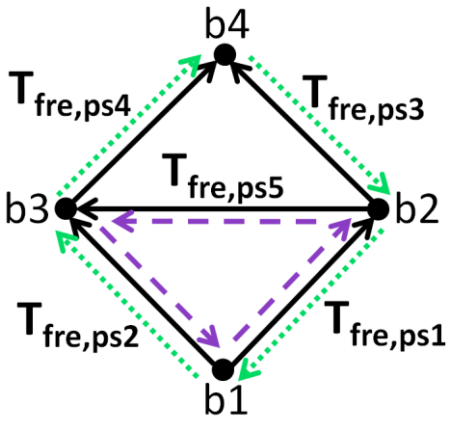

Figure 3.4: The two independent loops of the system graph

topology matrices in Eq. (3.11) are positive if the arrows that pertain to their corresponding freedom spaces point in the same directions as the colored arrows that specify the closed-loop paths shown in Fig. 3.4. Additionally, note that these signs are negative if the arrows point in opposite directions. The matrix in Eq. (3.11), [*FT*], is the system's freedom-topology matrix. This matrix always possesses as many rows as the number of independent closed-loop paths within the system multiplied by six. The matrix possesses as many columns as there are DOFs or independent twist vectors within each of the system's compliant joints (e.g., the parallel subsystems *ps1* through *ps5* in Fig. 2.21) summed together. For the example in this section (Fig. 3.1 to Fig. 3.5), the [*FT*] matrix can be determined by inserting the system's joint-freedom-topology matrices (e.g., Eqs. (3.2) and (3.4)) into Eq. (3.11) according to

$$[FT]=\begin{bmatrix}
-1 & 0 & 0 & 0 & 0 & 0 & 0 & 0 & 0 & 1 & 0 & 0 & 0 & 0 & 0 \\
0 & 0 & 0 & 0 & 1 & 0 & 0 & -1 & 0 & 0 & 0 & 0 & 0 & 0 & 0 \\
0 & -1 & 0 & 1 & 0 & 0 & -1 & 0 & 0 & 0 & 1 & 0 & 0 & 0 & 0 \\
0 & 0 & 0 & 0 & 0 & 1 & 0 & 0 & -1 & 0 & 0 & 0 & 0 & 0 & 0 \\
0 & -L/2 & -1 & -L/2 & 0 & 0 & -L/2 & 0 & 0 & 0 & L/2 & 1 & 0 & 0 & 0 \\
0 & 0 & 0 & 0 & L/2 & 0 & 0 & L/2 & 0 & 0 & 0 & 0 & 0 & 0 & 0 \\
1 & 0 & 0 & 0 & 0 & 0 & 0 & 0 & 0 & 0 & 0 & 0 & 1 & 0 & 0 \\
0 & 0 & 0 & 0 & -1 & 0 & 0 & 0 & 0 & 0 & 0 & 0 & 0 & 1 & 0 \\
0 & 1 & 0 & -1 & 0 & 0 & 0 & 0 & 0 & 0 & 0 & 0 & 0 & 0 & 0 \\
0 & 0 & 0 & 0 & 0 & -1 & 0 & 0 & 0 & 0 & 0 & 0 & 0 & -H & 0 \\
0 & L/2 & 1 & L/2 & 0 & 0 & 0 & 0 & 0 & 0 & 0 & 0 & H & 0 & 0 \\
0 & 0 & 0 & 0 & -L/2 & 0 & 0 & 0 & 0 & 0 & 0 & 0 & 0 & 0 & 1
\end{bmatrix} \tag{3.12}$$

where H is the length defined in Fig. 3.2. The **X** vector in Eq. (3.11) contains the system's velocity magnitude vectors, $\mathbf{x}_{ps1}$ through $\mathbf{x}_{ps5}$. The **X** vector is calculated by finding the null space of the system's [FT] matrix. The number of independent vector solutions that result by performing the null space of this matrix is the number of system DOFs, N, (i.e., the number of independent ways all the bodies within the system are compatible to move with respect to one another given their interconnected constraint topologies). For the example system in this chapter (Fig. 3.1 to Fig. 3.5), the null space of the matrix in Eq. (3.12) consists of three 15x1 **X** vector solutions (i.e., N=3).

To determine the freedom spaces of the rigid bodies within a general flexure system, all of the system's N independent **X** vectors must be multiplied by a path matrix, [P]. Path matrices always possess six rows and as many columns as there are DOFs or independent twist vectors within the system's compliant-joint freedom spaces summed together. Every component within a general path matrix is zero except for the components that correspond with the joint-freedom-topology matrices used in the chosen path from the ground to the body of interest. As an example, suppose we wished to identify the freedom space of the system's stage, labeled *b4* in Fig. 3.1. It is clear from the graph of Fig. 3.3 that one potential path starts from ground, *b1*, and progresses through the parallel subsystem *ps1* and then through *ps3* where it then ends at the system's stage, *b4*. This path's corresponding path matrix, $[P_{ps1,ps3}]$, is

$$\left[P_{ps1,ps3}\right] = \left[\left[jft\right]_{ps1} \quad [0] \quad \left[jft\right]_{ps3} \quad [0] \quad [0]\right]. \tag{3.13}$$

Another, option could be the path matrix, $[P_{ps2,ps5,ps3}]$, that corresponds with the path from the system's ground through *ps2*, then *ps5*, and finally *ps3* where it then ends at the system's stage. This path's matrix is

$$\left[P_{ps2,ps5,ps3}\right] = \left[\left[0\right] \quad \left[jft\right]_{ps2} \quad \left[jft\right]_{ps3} \quad \left[0\right] \quad -\left[jft\right]_{ps5}\right]. \tag{3.14}$$

Note that the sign of each joint-freedom-topology matrix corresponds with the graph's arrow convention and the path chosen as discussed previously. Once a potential path matrix that points from the system's ground to the body of interest is identified, the matrix should be multiplied by all N independent $\mathbf{X}$ vectors found from the null space of Eq. (3.11) to produce N twist vectors. These N twist vectors should then be linearly combined to generate the freedom space of the rigid body to which the path matrix pointed.

For the example in this section (Fig. 3.1 to Fig. 3.5), the stage's freedom space, $\mathbf{T}_{\mathbf{fre,b4}}$, was calculated using this approach. This freedom space, shown in Fig. 3.5, is the freedom space in Fig. 2.4 that consists of a black translation arrow that is perpendicular to a red plane of rotation lines that lies on the front face of the stage as shown. The freedom spaces of the two intermediate bodies, $\mathbf{T}_{\mathbf{fre,b2}}$ and $\mathbf{T}_{\mathbf{fre,b3}}$, can also be identified by multiplying all N independent $\mathbf{X}$ vectors with path matrices that point from ground to their respective bodies. These freedom spaces are also shown in Fig. 3.5. The freedom

space of *b2* is a red disk of rotation lines and the freedom space of *b3* is a single vertical red rotation line as shown.

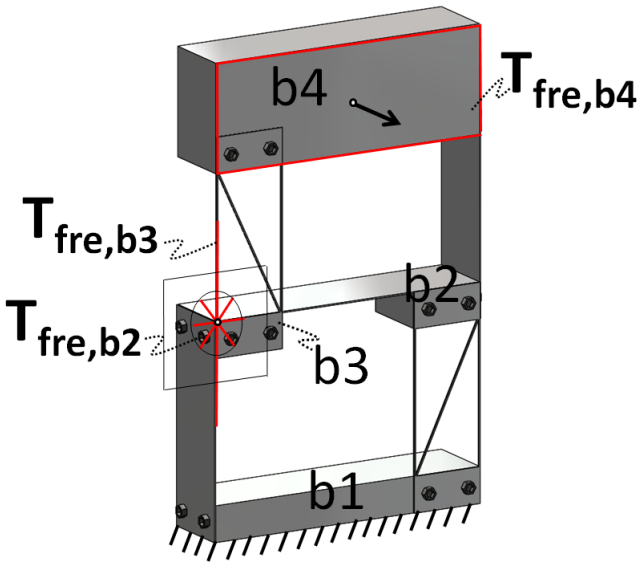

Figure 3.5 Freedom space of the system's bodies

Identifying the most efficient path from a general system's ground to its stage (or another body of interest) is a simple task to perform by inspection for the example system in this section. Suppose, however, we wished to calculate the freedom space of a particular body within a system that consisted of thousands of bodies joined together by compliant joints in an interconnected fashion (e.g., a lattice-based microarchitectured material). For this case, the adjacency matrix from graph theory [12-13] could be used in conjunction with the Dijkstra's algorithm [50] to enable an automated process for rapidly identify the most efficient path from ground to the desired body of interest. A system's adjacency matrix, [*A*], possesses as many rows and columns as there are nodes or vertices in

the system's graph. The component in row *h* and column *u* of the matrix is 1 if the body labeled *h* (i.e., *bh*) is joined to the body labeled *t* (i.e., *bu*) by a compliant joint. Otherwise, the component will be zero. The adjacency matrix, [*A*] of the graph in Fig. 3.3 is

$$[A]=\begin{bmatrix} 0 & 1 & 1 & 0 \\ 1 & 0 & 1 & 1 \\ 1 & 1 & 0 & 1 \\ 0 & 1 & 1 & 0 \end{bmatrix}. \tag{3.15}$$

Once the system's adjacency matrix has been identified, this matrix can be fed to the Dijkstra's algorithm to find the shortest path between the vertex that corresponds with the grounded body and the vertex that corresponds with the rigid body of interest. This path can then be used to generate the best path matrix for rapidly calculating the body's freedom space.

Thus, the systematic mobility analysis approach of this section is summarized by the following seven steps:

Step 1: Identify the freedom spaces of a system's compliant or rigid joints.

Step 2: Use these freedom spaces to create their corresponding joint-freedom-topology matrices (i.e., $[jft]_{pse}$).

Step 3: Construct the incidence matrix, [*C*], using a simplified graph of the system.

Step 4: Construct the system's freedom-topology matrix, [*FT*], by inserting the matrices of Step 2 into their corresponding columns within the transpose of the left null space of the matrix in Step 3.

Step 5: Find the system's *N* independent **X** vectors by taking the null space of [*FT*] from Step 4.

Step 6: Use the system's adjacency matrix, [*A*], in conjunction with Dijkstra's algorithm to construct the optimal path matrix, [*P*], that leads from the system's ground to the body of interest (usually the stage).

Step 7: Multiply the path matrix in Step 6 with all *N* of the **X** vectors from Step 5 and to generate the freedom space of the stage. In other words, $\mathbf{T}_{\mathbf{fre,stage}} = \mathbf{PX}$.

Note that although the freedom spaces of the compliant joints, *ps1* through *ps5*, of the case study of Fig. 3.1 are all the same type of freedom space, the approach of this research works for general systems with any variety of different compliant-joint freedom spaces.

3.2 Constraint-space-based Approach to Mobility Analysis

This section introduces an alternate but complementary constraint-space-based approach to the freedom-space-based approach introduced in section 3.1 for performing the mobility analysis of general flexure systems. Another way to determine the freedom space of a flexure system's stage is to first identify the constraint spaces of each set of flexure elements (i.e., compliant joints) that join the system's rigid bodies together. The respective constraint spaces, $\mathbf{W}_{\mathbf{con,ps1}}$ through $\mathbf{W}_{\mathbf{con,ps5}}$, of the compliant joints, *ps1* through *ps5*, in the example of Fig. 2.21 can each be calculated by individually inserting their complementary freedom spaces, $\mathbf{T}_{\mathbf{fre,ps1}}$ (i.e., Eq. (3.1)) through $\mathbf{T}_{\mathbf{fre,ps5}}$, found previously and depicted in Fig. 3.1, into Eq. (2.7). These resulting constraint spaces coincidentally

look similar to their complementary freedom spaces (Fig. 3.1) except for the fact that their planes are blue instead of red because they consist of force lines instead of rotation lines, and they possess orthogonal black moment lines with circular arrows about their axes instead of black translation arrows (Fig. 2.4 and Fig. 2.5). Thus, for the same coordinate system shown in Fig. 3.2 but with the independent twist vectors labeled $\mathbf{T_1}$ though $\mathbf{T_6}$ replaced by independent wrench vectors labeled $\mathbf{W_1}$ though $\mathbf{W_6}$, the constraint space of *ps1*, $\mathbf{W_{con,ps1}}$, can be mathematically modeled in a fashion similar to Eq. (3.1)

$$\mathbf{W_{con,ps1}} = \sum_{i=1}^{n=3} \mathbf{W_i} = f_1 \begin{bmatrix} 1 \\ 0 \\ 0 \\ 0 \\ 0 \\ 0 \end{bmatrix} + f_2 \begin{bmatrix} 0 \\ 0 \\ 1 \\ 0 \\ L/2 \\ 0 \end{bmatrix} + \tau_3 \begin{bmatrix} 0 \\ 0 \\ 0 \\ 0 \\ 1 \\ 0 \end{bmatrix} = \left[jct \right]_{ps1} \mathbf{y_{ps1}} \tag{3.16}$$

where $\mathbf{T_{fre,ps1}}$ is replaced by $\mathbf{W_{con,ps1}}$, n is replaced by m, i is replaced by j, $\mathbf{T_i}$ is replaced by $\mathbf{W_j}$, ω_1 is replaced by f_1, ω_2 is replaced by f_2, v_3 is replaced by τ_3, $[jft]_{ps1}$ is replaced by $[jct]_{ps1}$, and $\mathbf{x_{ps1}}$ is replaced by $\mathbf{y_{ps1}}$. The matrix $[jct]_{ps1}$ is called the joint-constraint-topology matrix of the parallel subsystem *ps1* and is defined in a fashion similar to Eq. (3.2)

$$\left[jct \right]_{ps1} = \begin{bmatrix} 1 & 0 & 0 & 0 & 0 & 0 \\ 0 & 0 & 1 & 0 & L/2 & 0 \\ 0 & 0 & 0 & 0 & 1 & 0 \end{bmatrix}^T \tag{3.17}$$

where $[jft]_{ps1}$ is replaced by $[jct]_{ps1}$, and $\mathbf{y_{ps1}}$ is the load magnitude vector of *ps1* defined in a fashion similar to Eq. (3.3)

$$\mathbf{y_{ps1}} = \begin{bmatrix} f_1 & f_2 & \tau_3 \end{bmatrix}^T \tag{3.18}$$

where $\mathbf{x_{ps1}}$ is replaced by $\mathbf{y_{ps1}}$, and ω_1, ω_2, and v_3 are replaced by f_1, f_2, and τ_3 respectively. Thus, by identifying the *m* independent wrench vectors within each compliant joint's constraint space, all the system's joint-constraint-topology matrices, $[jct]_{ps1}$ through $[jct]_{ps5}$, can be constructed similar to the system's joint-freedom-topology matrices, $[jft]_{ps1}$ through $[jft]_{ps5}$, in section 3.1.

Note that, unlike the example of in section 3.1, the constraint spaces of most flexure-systems' compliant joints are significantly different in appearance from their complementary freedom spaces (e.g., Figs. 2.7, Fig. 2.8, Fig. 2.11, and Fig. 2.12). Furthermore, these constraint spaces typically consist of different numbers, *m*, of independent wrench vectors than the numbers of independent twist vectors, *n*=6-*m*, that constitute their complementary freedom spaces. Thus, their 6x*n* joint-freedom-topology matrices and their 6x*m* joint-constraint-topology matrices are typically different sizes and consist of different components. The case study example in section 3.1 with coincidentally identical joint-freedom-topology matrices and joint-constraint-topology matrices was selected to simplify the mathematics and to condense the length of this thesis.

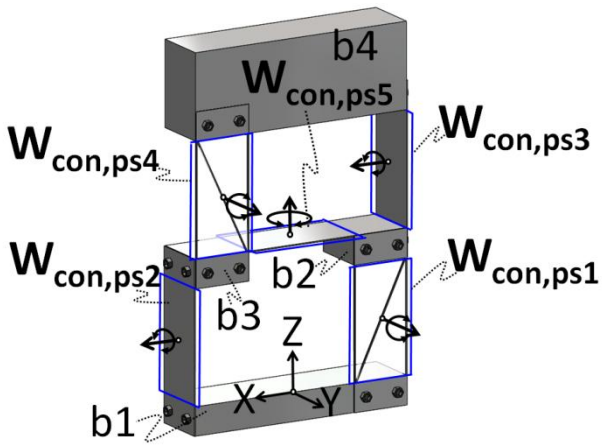

Figure 3.6: Constraint spaces of each parallel subsystem within flexure system

Once all the system's joint-constraint-topology matrices, $[jct]_{ps1}$ through $[jct]_{ps5}$, and their corresponding load magnitude vectors, $\mathbf{y}_{ps1}$ through $\mathbf{y}_{ps5}$, have been constructed, they can be used to calculate the freedom space of the system's stage. To do this, imagine loading each of the system's rigid bodies, labeled *b1* through *b4* in Fig. 3.6, with external wrench vectors, $\mathbf{W}_{b1}$ through $\mathbf{W}_{b4}$ respectively. For the flexure system to be in static equilibrium, the compliant joints surrounding each of the system's rigid bodies would need to resist their corresponding external load. In other words, the external loads imparted on each rigid body subtracted by the loads within their surrounding parallel-subsystem constraint spaces must equal zero according to

$$\begin{array}{lllllllll} \mathbf{W}_{b1} & - & \mathbf{W}_{con,ps1} & - & \mathbf{W}_{con,ps2} & & & = & \mathbf{0} \\ \mathbf{W}_{b2} & + & \mathbf{W}_{con,ps1} & - & \mathbf{W}_{con,ps3} & - & \mathbf{W}_{con,ps5} & = & \mathbf{0} \\ \mathbf{W}_{b3} & + & \mathbf{W}_{con,ps2} & - & \mathbf{W}_{con,ps4} & + & \mathbf{W}_{con,ps5} & = & \mathbf{0} \\ \mathbf{W}_{b4} & + & \mathbf{W}_{con,ps3} & + & \mathbf{W}_{con,ps4} & & & = & \mathbf{0} \end{array} \tag{3.19}$$

where the signs associated with the constraint spaces of each parallel subsystem are determined by the direction of the arrows established in the convention of the system's graph shown in Fig. 3.7 where the edges are labeled $\mathbf{W}_{\mathbf{con,p1}}$ through $\mathbf{W}_{\mathbf{con,p5}}$. Just as Eq. (3.6) can be reformulated as Eq. (3.7) in section 3.1, Eq. (3.19) can also be reformulated according to

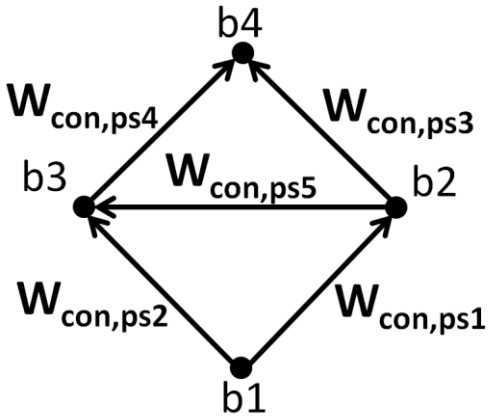

Figure 3.7: Graphical representation of a system with edges as constraint spaces

$$\begin{bmatrix} -[jct]_{ps1} & -[jct]_{ps2} & [0] & [0] & [0] \\ [jct]_{ps1} & [0] & -[jct]_{ps3} & [0] & -[jct]_{ps5} \\ [0] & [jct]_{ps2} & [0] & -[jct]_{ps4} & [jct]_{ps5} \\ [0] & [0] & [jct]_{ps3} & [jct]_{ps4} & [0] \end{bmatrix} \begin{bmatrix} \mathbf{y}_{\mathbf{ps1}} \\ \mathbf{y}_{\mathbf{ps2}} \\ \mathbf{y}_{\mathbf{ps3}} \\ \mathbf{y}_{\mathbf{ps4}} \\ \mathbf{y}_{\mathbf{ps5}} \end{bmatrix} = [CT]\mathbf{Y} = \begin{bmatrix} -\mathbf{W}_{\mathbf{b1}} \\ -\mathbf{W}_{\mathbf{b2}} \\ -\mathbf{W}_{\mathbf{b3}} \\ -\mathbf{W}_{\mathbf{b4}} \end{bmatrix} \tag{3.20}$$

where [*CT*] is called the system's constraint-topology matrix and **Y** is a vector that contains the system's load magnitude vectors, $\mathbf{y}_{\mathbf{ps1}}$ though $\mathbf{y}_{\mathbf{ps5}}$. Note that a system's [*CT*] matrix contains as many rows as there are rigid bodies within the system multiplied by six and as many columns as the number of independent wrench vectors within each of the system's compliant-joint constraint spaces summed

together. The sign of each joint-constraint-topology matrix within the system's constraint-topology matrix is positive if its corresponding arrow in the graph of Fig. 3.7 points into the rigid body that corresponds with the row within which the join-constraint-topology matrix resides in the [*CT*] matrix. Otherwise, if the arrow points away from the rigid body, the sign is negative. It is most significant to note that the [*CT*] matrix defined in Eq. (3.20) is the transpose of the system's incidence matrix defined in Eq. (3.8) with the system's joint-constraint-topology matrices, $[jct]_{ps1}$ through $[jct]_{ps5}$, inserted within their respective columns. This observation is not coincidental to this example, but is true for all flexure systems.

The constraint space of any desired rigid body in a system can be calculated using the system's constraint-topology matrix after at least one rigid body has been chosen as the system's fixed ground. Suppose, for instance, we wished to calculate the constraint space of the system's stage, *b4*, in the example of Fig. 3.6, where body *b1* is the fixed ground. To do this, imagine only loading the body of interest, (i.e., the stage) with an external wrench vector, $\mathbf{W_{b4}}$. To maintain static equilibrium, the grounded body, *b1*, would be loaded with an equal but opposite wrench vector $\mathbf{W_{b1}}=-\mathbf{W_{b4}}$ to keep it from moving. Since the other bodies within the system are not loaded, $\mathbf{W_{b2}}$ and $\mathbf{W_{b3}}$ in Eq. (3.20) are zero vectors. If we then eliminate the rows within Eq. (3.20) that do not correspond with those unloaded bodies, the resulting equation is

$$\begin{bmatrix} [jct]_{ps1} & [0] & -[jct]_{ps3} & [0] & -[jct]_{ps5} \\ [0] & [jct]_{ps2} & [0] & -[jct]_{ps4} & [jct]_{ps5} \end{bmatrix} \begin{bmatrix} \mathbf{y}_{ps1} \\ \mathbf{y}_{ps2} \\ \mathbf{y}_{ps3} \\ \mathbf{y}_{ps4} \\ \mathbf{y}_{ps5} \end{bmatrix} = [B_{b2,b3}]\mathbf{Y}_{b2,b3} = \mathbf{0} \tag{3.21}$$

where $[B_{b2,b3}]$ is called a rigid-body matrix that only contains the rows in the system's constraint-topology matrix that corresponds with body *b2* and *b3* in the system, and $\mathbf{Y}_{b2,b3}$ is the null space of that particular rigid-body matrix. The number of independent vectors within that null space, *M*, is the number of independent load-magnitude combinations that could be imposed throughout the compliant joint topology of the system to keep bodies *b2* and *b3* in static equilibrium in response to the loaded body of interest. Thus, if another rigid-body matrix, $[B_{b4}]$ is extracted from the row within the system's constraint-topology matrix (i.e., Eq. (3.20)) that corresponds with the loaded body of interest (i.e., the stage *b4*) according to

$$[B_{b4}] = \begin{bmatrix} [0] & [0] & [jct]_{ps3} & [jct]_{ps4} & [0] \end{bmatrix} \tag{3.22}$$

and this matrix is multiplied by all *M* of these independent vectors, $\mathbf{Y}_{b2,b3}$, another set of independent vectors are generated. If the resulting *M* vectors are linearly combined, the constraint space of the stage, $\mathbf{W}_{con,b4}$, is determined. Note from the last row's corresponding equation in Eq. (3.20) that the load $\mathbf{W}_{b4}$ applied to the stage must lie within the stage's constraint space, $\mathbf{W}_{con,b4}$, for the system to achieve static equilibrium. This insight is further confirmed by the fact that the theory of this paper

models flexure elements as ideal constraints that can only impart loads in certain directions but not in others. Once the constraint space of the stage, $\mathbf{W}_{\mathbf{con,b4}}$, is known, Eq. (2.7) can be used to calculate the stage's freedom space, $\mathbf{T}_{\mathbf{fre,b4}}$, to complete the system's mobility analysis.

The systematic constraint-space-based mobility analysis approach can thus be summarized according to the following steps:

Step 1: Identify the constraint spaces of a system's compliant or rigid joints.

Step 2: Use these constraint spaces to create their corresponding joint-constraint-topology matrices (i.e., $[jct]_{pse}$).

Step 3: Construct the incidence matrix, [*C*], using a simplified graph of the system.

Step 4: Construct the system's constraint-topology matrix, [*CT*], by inserting the matrices of Step 2 into their corresponding columns within the transpose of the matrix in Step 3.

Step 5: Create a rigid-body matrix, [*B*], containing the rows of the [*CT*] matrix from Step 4 that correspond with the system's bodies that are not the chosen ground and body of interest (usually the stage).

Step 6: Find the *M* independent **Y** vectors that constitute the null space of the rigid-body matrix from Step 5, and then multiply all of these vectors with another rigid-body matrix, $[B_{body\text{-}of\text{-}interest}]$, containing the row of the [*CT*] matrix from Step 4 that corresponds with the body of interest. In short, the relation can be expressed as $\mathbf{W}_{\mathbf{con,stage}} = \mathbf{BY}$.

Step 7: Linearly combine the resulting *M* wrench vectors from Step 6 to generate the constraint space of the body of interest and then use Eq. (2.7) to calculate the body's complementary freedom space.

3.3 Constraint analysis of flexure systems

This section introduces a new way to utilize the principles of section 3.1 and 3.2 to rapidly perform the constraint analysis of general flexure systems—including those that are interconnected hybrid. Constraint analysis is the process by which designers determine whether a flexure system is under-constrained or not and whether the system is over-constrained or exactly-constrained. Both of these constraint characteristics depend on which bodies within the system are chosen as the system's stage, intermediate bodies, and ground.

A system is under-constrained [2,38,51] if it possesses intermediate bodies that are not fully constrained (i.e., the intermediate bodies possess unconstrained DOFs) when the system's chosen stage is held fixed with respect to its chosen ground. Under-constraint occurs when subsystem's stacked in series possess redundant DOFs. Although an under-constrained system can typically achieve larger ranges of motion without yielding, such systems are prone to unwanted vibrations along directions that cannot be controlled by system actuators.

A system is over-constrained [2,38,51] if it possess elements or subsystems that are redundant (i.e., they do the same job of constraining a particular DOF or set of DOFs as another element or subsystem within the system). A system is exactly-constrained if it is not over-constrained. Although

over-constrained systems can exhibit some beneficial characteristics (e.g., increased symmetry, thermal stability, stiffness, and load capacity), exactly-constrained systems are preferable for precision applications where repeatability is of greatest importance.

A general system is not under-constrained if the number of independent twist vectors within the freedom space of its stage equals the number of system DOFs (i.e., N independent $\mathbf{X}$ vectors defined in Eq. (3.11) from section 3.1). If N is larger than this number, the system is under-constrained. The system in Fig. 3.5 is not under-constrained if *b4* is chosen as its stage and *b1* is chosen as its ground because the freedom space of *b4* possesses three independent twist vectors and N=3 in the example system. Thus, if *b4* is held fixed with respect to the ground *b1*, the system's other rigid bodies are also unable to move. If, however, *b3* is defined as the system's new stage and *b1* remains its ground, the system would be under-constrained because the freedom space of *b3* only possesses one independent twist vector. Thus, if *b3* is held fixed with respect to the ground *b1*, two other system DOFs will remain unconstrained allowing *b2* and *b4* to move in an uncontrolled way. Note that no rigid-body freedom space can ever possess more independent twist vectors than system DOFs (i.e., N) and N minus the number of independent twist vectors within the freedom space of the system's chosen stage will be the number of system DOFs that are not properly constrained.

A general system is exactly-constrained if the number of independent wrench vectors within the constraint space of its stage equals the number of independent wrench vectors, M, within the null space, $\mathbf{Y}$, of the rigid-body matrix defined in Eq. (3.21) from section 3.2 that contains the rows of the

system's constraint-topology matrix that correspond with the system's intermediate rigid bodies (i.e., not its stage and ground). If *M* is larger than the number of independent wrench vectors within the chosen stage's constraint space, the system is over-constrained. The system in Fig. 3.5 is exactly-constrained if *b4* is chosen as its stage and *b1* is chosen as its ground because the constraint space of *b4* possesses three independent wrench vectors and *M*=3 in the example system. If *b3* is defined as the system's new stage and *b1* remains its ground, the system would still be exactly-constrained because the constraint space of *b3* possesses five independent wrench vectors and the new system's *M* would also be five. Note that no rigid-body constraint space can possess more independent wrench vectors than *M* and *M* minus the number of independent wrench vectors within the constraint space of the system's chosen stage is the number of redundant constraints in the system.

CHAPTER 4

Synthesis of Flexure Systems with Screw Algebra and Graph Theory

This chapter introduces a systematic synthesis approach of flexure systems of any configuration and complexity—including and especially interconnected hybrid flexure systems. The method is based on the screw and graph theory analysis method in chapter 3. Three case studies are provided to demonstrate the steps of the synthesis approach.

The synthesis approach is an extension of the analysis method introduced in the previous section. When performing analysis, the [FT] matrix is given, and the [X] matrix is solved for to find the motion of the entire system. Conversely, when performing synthesis, the [FT] matrix is the unknown to be solved for, and the information given is the desired output motion and the actuator input motion. The given information is interpreted as parts of the [FT] and [X] matrices, and then a [FT] compatible that satisfies the given design constraints is pieced together for. Three case studies are detailed to guide through the synthesis approach.

4.1 Case study 1: Design of a transmission flexure system that doubles a rotation on the same axis

Suppose that in a Cartesian coordinates frame, a rotation about the z-axis is given as the input, and an output rotation about the same axis with twice the magnitude is desired. A six-step synthesis process as follows is used to design a flexure system that achieves this desired function:

Step 1: Identify desired motion and design requirements. The desired motions are interpreted as twist vectors, where the input is $[0 \quad 0 \quad 0 \quad \omega \quad 0 \quad 0]^T$, and the output is $[0 \quad 0 \quad 0 \quad 2\omega \quad 0 \quad 0]^T$. No additional design requirements are present in this case study.

Step 2: Choose a Graph. The graph indicates the number of rigid bodies and flexure elements in the system and the manner that they are arranged. The graph in Fig. 4.1 is chosen for this case study, where the vertices are labeled be through *b4*, representing the rigid bodies in the system, and *b1* is the ground, *b2* the input, and *b4* is the output stage; the edges are labeled *e1* through *e5*, representing the flexure elements in the system. The number of rigid bodies and flexure elements is thus decided when selecting the graph.

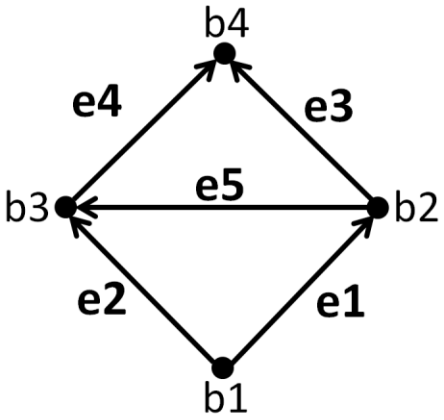

Figure 4.1: A chosen system graph for a transmission flexure

Several rules of thumb are outlined and to be used as guidelines in the selection of a graph: 1) Select the simplest graph with as few elements as possible. Having the least number of rigid stages

and flexure elements reduces the complexity of the system, and thereby may reduce cost and improve manufacturability. 2) Select symmetric graphs if possible. Symmetry is often preferred as it may offer many advantages. A system cannot be symmetric if the graph itself is not symmetric as the numbers of rigid stages and flexure elements renders symmetry impossible. 3) In order to avoid under-constraint, identical freedom spaces or sub-freedom spaces of edges should be able to be found in separate loops. Identical freedom spaces or freedom subspaces in the same loop will cause solutions found later in the synthesis process to have equal and opposite magnitudes even if other bodies are held fixed resulting in rigid bodies being under-constrained.

For this case study, the input and output are rotations about the same axis, and therefore have the same freedom space. It is impossible to employ only one loop and at the same time keep the edges from having overlapping sub-freedom spaces, hence the graph in Fig. 4.1 is the simplest graph for the desired function in this case study.

Step 3: Construct the governing equation [FT][X] = 0. The exact forms of each individual [*jft*] matrix are unknown in this step, however their placements within [**FT**] are known from the chosen graph. For this case study, the graph in Fig. 4.1 yields:

$$[\mathbf{FT}][\mathbf{X}]=\begin{bmatrix}[jft]_{e1} & -[jft]_{e2} & 0 & 0 & [jft]_{e5}\\ 0 & 0 & [jft]_{e3} & -[jft]_{e4} & -[jft]_{e5}\end{bmatrix}\begin{bmatrix}\mathbf{x_1}\\ \mathbf{x_2}\\ \mathbf{x_3}\\ \mathbf{x_4}\\ \mathbf{x_5}\end{bmatrix}=0 \qquad (4.1)$$

where $[jft]_{ei}$ correspond to edge *i*, and their placement is determined by visual inspection of independent loops in the graph of Fig. 4.1. The number of column in the [**X**] matrix is the number of DOF in the system, which equals to 1 for this case study. The independent two loops selected in Eq. (4.1) are loop *e1-e2-e5* and loop *e3-e4-e5*. Note that while selecting different loops will lead to the same mathematical solutions, but some loops may be easier to solve than others depending on the structure of the governing equation.

Step 4: Interpret the desired motion as components of the governing equation. In this case study, since *e1* is the path between the ground and the input, and should have a freedom space that allows the input z-axis rotation, the input is interpreted as $[jft]_{e1} = [0 \quad 0 \quad 1 \quad 0 \quad 0 \quad 0]^T$ and $\mathbf{x_1} = 1$. A path can be traced from the ground to the output through *e1* and *e3*, in order to satisfy the output having twice the magnitude, a relation is obtained according to

$$[jft]_{e1}\mathbf{x}_1 + [jft]_{e3}\mathbf{x}_3 = [0 \quad 0 \quad 2 \quad 0 \quad 0 \quad 0]^T \tag{4.2}$$

which yields a possible solution set of $[jft]_{e3} = [0 \quad 0 \quad 1 \quad 0 \quad 0 \quad 0]^T$ and $\mathbf{x_3} = 1$.

Step 5: Find possible solutions to the governing equation. Substitute $[jft]_{e1}$, $[jft]_{e3}$, $\mathbf{x_1}$,and $\mathbf{x_3}$ into [**FT**] and [**X**] matrices into the governing equation and solve for compatible [*jft*] matrices for each edge of the graph in Fig. 4.1. For a general flexure system, as well as for this case study, there are many possible solutions in the design space. All possible designs can be evaluated and selected at

the designer's discretion, based on criterions such as design constraints, manufacture capability and/or more.

For this case study, a pure translation in the x-direction is chosen at random as a design choice for *e5* since it is simple to visualize and easy to implement. The motion can be expressed as $[jft]_{e5} = [0 \quad 0 \quad 0 \quad 1 \quad 0 \quad 0]^T$ with $\mathbf{x}_5$ remaining to be solved. Substituting $[jft]_{e5}$ into Eq. (4.1), the loop through *e1-e2-e5* is expressed according to

$$\begin{bmatrix}[jft]_{e1} & -[jft]_{e2} & [jft]_{e5}\end{bmatrix}\begin{bmatrix}\mathbf{x_1}\\ \mathbf{x_2}\\ \mathbf{x}_5\end{bmatrix} = \begin{bmatrix}\begin{bmatrix}0\\0\\1\\0\\0\\0\end{bmatrix} & -[jft]_{e2} & \begin{bmatrix}0\\0\\0\\1\\0\\0\end{bmatrix}\end{bmatrix}\begin{bmatrix}1\\ \mathbf{x_2}\\ \mathbf{x}_5\end{bmatrix} = \mathbf{0} \tag{4.3}$$

Infinite sets of solutions exists for $[jft]_{e2}$, $\mathbf{x}_2$ and $\mathbf{x}_5$, and the simplest solution set for Eq. (4.3) is

$$\begin{bmatrix}[jft]_{e1} & -[jft]_{e2} & [jft]_{e5}\end{bmatrix}\begin{bmatrix}\mathbf{x_1}\\ \mathbf{x_2}\\ \mathbf{x}_5\end{bmatrix} = \begin{bmatrix}\begin{bmatrix}0\\0\\1\\0\\0\\0\end{bmatrix} & -\begin{bmatrix}0\\0\\1\\d\\0\\0\end{bmatrix} & \begin{bmatrix}0\\0\\0\\1\\0\\0\end{bmatrix}\end{bmatrix}\begin{bmatrix}1\\1\\d\end{bmatrix} = \mathbf{0} \tag{4.4}$$

where d is an arbitrary distance. It can be seen from Eq. (4.4) that $[jft]_{e2} = [0 \quad 0 \quad 1 \quad d \quad 0 \quad 0]^T$, $\mathbf{x}_2 = 1$, and $\mathbf{x}_5 = d$, the motion of this solution set is a rotation parallel to the z-axis with a coupled translation

in the x-direction. Decomposing the twist vector of $[jft]_{e2}$ shows that the axis of rotation is parallel to the z-axis and located at distance of d to the positive x-direction from the coordinates frame origin.

Another solution to the governing equation can be obtained by adding a DOF to the vector space already spanned by the know twist vectors within the loop. One of the many possible solution set for $[jft]_{e2}$ is

$$[jft]_{e2}\mathbf{x}_2 = \begin{bmatrix} 0 & 1 \\ 0 & 0 \\ 1 & 0 \\ d & 0 \\ 0 & 0 \\ 0 & 0 \end{bmatrix} \begin{bmatrix} 1 \\ 0 \end{bmatrix} \tag{4.5}$$

where $\mathbf{x}_5 = d$. Note that in the solution provided in Eq. (4.5) the additional DOF added to $[jft]_{e2}$ is linearly independent to all other twist vectors within the loop, and therefore its associated magnitude can only be 0 in order to satisfy the governing equation of Eq. (4.1). The added DOF is locked up by the other flexure elements in the loop, and has no impact on the kinematics of the system. A different motion may have been added to $[jft]_{e2}$ for a different solution set, and more motions can be added to $[jft]_{e2}$ to obtain solution sets with higher DOF. Some examples are

$$[jft]_{e2}\mathbf{x}_2 = \begin{bmatrix} 0 & 1 & 0 \\ 0 & 0 & 0 \\ 1 & 0 & 0 \\ d & 0 & 0 \\ 0 & 0 & 1 \\ 0 & 0 & 0 \end{bmatrix} \begin{bmatrix} 1 \\ 0 \\ 0 \end{bmatrix} \tag{4.6}$$

$$[jft]_{e2}\mathbf{x}_2 = \begin{bmatrix} 0 & 1 & 0 & 0 \\ 0 & 0 & 0 & 1 \\ 1 & 0 & 0 & 0 \\ d & 0 & 0 & 0 \\ 0 & 0 & 1 & 0 \\ 0 & 0 & 0 & 0 \end{bmatrix} \begin{bmatrix} 1 \\ 0 \\ 0 \\ 0 \end{bmatrix} \tag{4.7}$$

$$[jft]_{e2}\mathbf{x}_2 = \begin{bmatrix} 0 & 1 & 0 & 0 & 0 \\ 0 & 0 & 1 & 0 & 0 \\ 1 & 0 & 0 & 0 & 0 \\ d & 0 & 0 & 0 & 0 \\ 0 & 0 & 0 & 1 & 0 \\ 0 & 0 & 0 & 0 & 1 \end{bmatrix} \begin{bmatrix} 1 \\ 0 \\ 0 \\ 0 \\ 0 \end{bmatrix} \tag{4.8}$$

where $\mathbf{x}_5$ = d for all of the above solution sets. Each column of the [*jft*] matrices represents the motions allowed by the corresponding flexure element, for this case study $[jft]_{e2}$ can have up to 5 DOFs as indicated in the solution set of Eq. (4.8).

Note that in the possible solutions for $[jft]_{e2}$, the freedom space of the solution set with the least DOF is a subspace of the freedom spaces all other solution sets, indicating that the solution with the least DOF contains the motions that all other solutions must have. By using the relation of Eq. (2.7), constraint spaces corresponding to each freedom space of the solution sets can be found, and the

constraint space of the solution set with the least DOC is a subspace of the constraint spaces of all other solution sets, indicating that the solution with the least DOC and hence most DOF contains the constraining actions that all other solution sets must have. When selecting from one of the possible solutions, designers may first identify solutions with the least and most DOF, and search for solutions containing the necessary freedom and constraint spaces in the FACT library. Also note that since $[jft]_{e5}$ is a design choice made at the beginning of step 5 instead of a design requirement, the DOFs of $[jft]_{e2}$ and $[jft]_{e5}$ can be interchanged and still satisfy Eq. (4.1), resulting in different designs. Extra DOFs may also be added to $[jft]_{e1}$ as long as no redundant DOF is created after solving the governing equation. For this case study, interchanging or adding DOFs are unnecessary.

With one of the loops in the flexure system solved, to find solutions for remaining unknowns in the flexure system, substitute $[jft]_{e5}$ and $\mathbf{x}_5$ into loop *e3-e4-e5* and we have

$$\left[\begin{bmatrix}0\\0\\1\\0\\0\\0\end{bmatrix} - [jft]_{e4} \begin{bmatrix}0\\0\\0\\1\\0\\0\end{bmatrix}\right]\begin{bmatrix}1\\\mathbf{x}_4\\d\end{bmatrix} = \mathbf{0} \tag{4.9}$$

The same process can be applied to find possible solution sets for $[jft]_{e4}$ and $\mathbf{x}_4$, where the possible solution set with the least DOF is $[jft]_{e4}\mathbf{x}_4 = [0 \quad 0 \quad 1 \quad -d \quad 0 \quad 0]^T[1]$, and the solution set with the most DOF is

$$[jft]_{e4}\mathbf{x}_4 = \begin{bmatrix} 0 & 1 & 0 & 0 & 0 \\ 0 & 0 & 1 & 0 & 0 \\ 1 & 0 & 0 & 0 & 0 \\ -d & 0 & 0 & 0 & 0 \\ 0 & 0 & 0 & 1 & 0 \\ 0 & 0 & 0 & 0 & 1 \end{bmatrix} \begin{bmatrix} 1 \\ 0 \\ 0 \\ 0 \\ 0 \end{bmatrix} \tag{4.10}$$

For this case study, both $[jft]_{e2}$ and $[jft]_{e4}$ needs to allow at least one translation and at least provide one constraining force. Solution sets chosen for $[jft]_{e2}$ and $[jft]_{e4}$ are given as follows

$$[jft]_{e2} = \begin{bmatrix} 0 & 1 & 0 \\ 0 & 0 & 0 \\ 1 & 0 & 0 \\ d & 0 & 0 \\ 0 & 0 & 1 \\ 0 & -d & 0 \end{bmatrix} \tag{4.11}$$

$$[jft]_{e4} = \begin{bmatrix} 0 & 1 & 0 \\ 0 & 0 & 0 \\ 1 & 0 & 0 \\ -d & 0 & 0 \\ 0 & 0 & 1 \\ 0 & d & 0 \end{bmatrix} \tag{4.12}$$

These solutions are chosen because they can be easily implemented as blade flexures.

Step 6: Interpret joint freedom topology matrices as flexure elements or flexure subsystems using FACT. With all [*jft*] and hence freedom space of the flexure elements determined, the flexure

system can now be built by interpreting the matrices into flexure elements using FACT.

The motion of $[jft]_{e1}$ is a rotation about the z-axis, according to FACT the corresponding freedom space is a red line through the z-axis, and the constraint space is a set of blue planes intersecting at the z-axis, which can be achieved by a set of intersecting blade flexure as shown in Fig. 4.2. Likewise, $[jft]_{e3}$ also indicates a rotation about the z-axis, and can also be achieved by a set of blade flexures intersecting the z-axis as shown in Fig. 4.3. The two subsystems of $[jft]_{e1}$ and $[jft]_{e3}$ are connected in

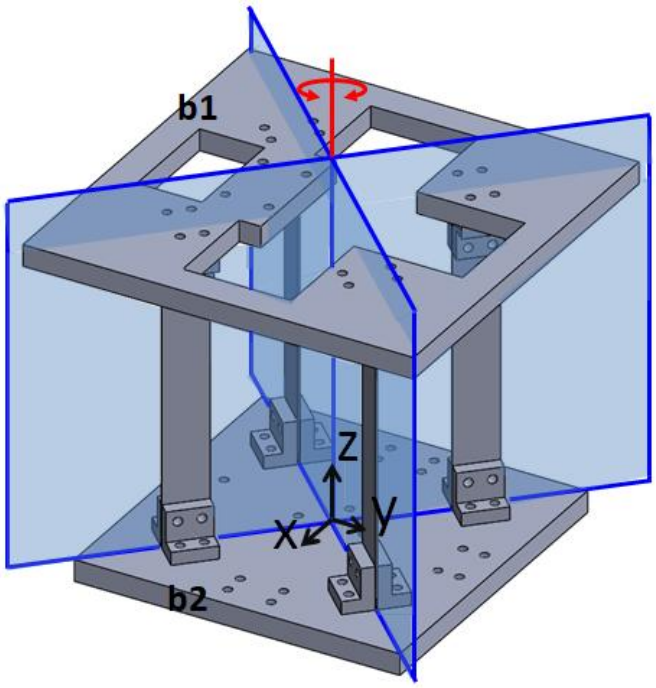

Figure 4.2: Implementation of $[jft]_{e1}$ of a 1 DOF transmission flexure system

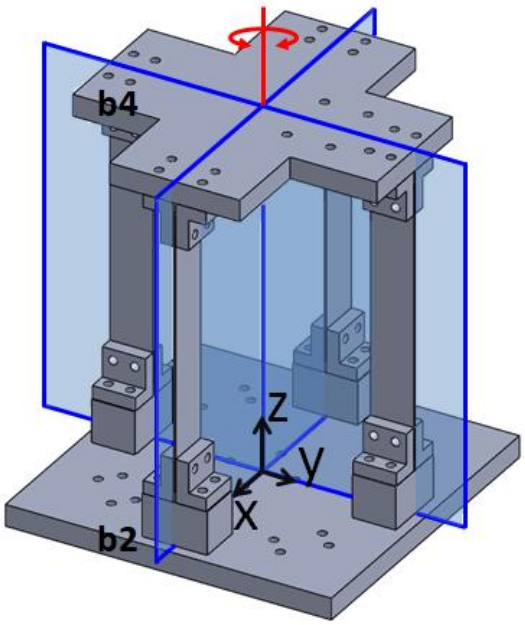

Figure 4.3: Implementation of $[jft]_{e3}$ of a 1 DOF transmission flexure system

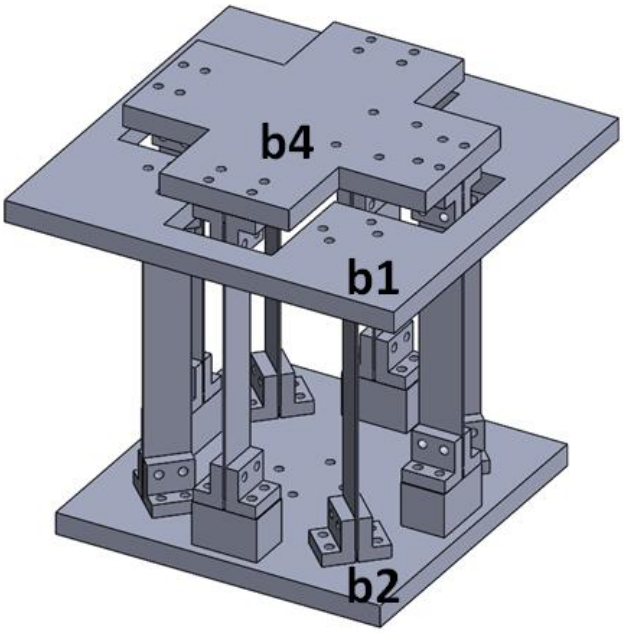

Figure 4.4: Placement of flexure for *e1* and *e3* of a 1 DOF transmission flexure system

a serial configuration as shown in Fig. 4.4. The motion of $[jft]_{e5}$ is a pure translation in the x-direction, and according to FACT it has a constraint space of a set of parallel blue plane, which can be achieved by a set of parallel blade flexures as shown in Fig. 4.5. Finally, both of the constraint spaces of $[jft]_{e2}$ and $[jft]_{e4}$ are a single blue plane, allowing two rotations and one translation, and can be achieved by a blade flexure placed in the position shown in Fig. 4.6 and Fig. 4.7. The placement of the flexures of *e2*, *e4* and *e5* connecting *b1*, *b2*, *b3* and *b4* is shown in Fig. 4.8. Connecting all the flexure subsystems, the complete flexure system is shown in Fig. 4.9.

Frequency modal analysis is performed with SOLIDWORKS to validate the design. The first natural frequency modeshape is as shown in Fig. 4.10. The FEA results confirm that the stage rotates twice as much as the input body.

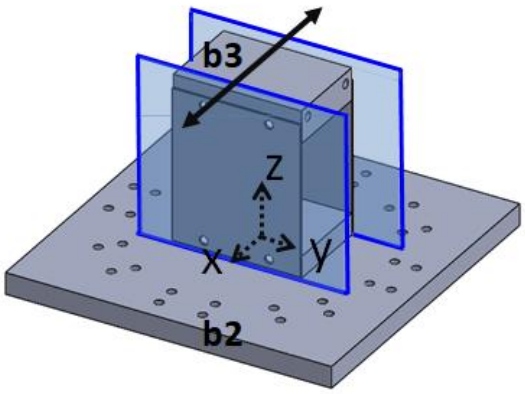

Figure 4.5: Implementation of $[jft]_{e5}$ of a 1 DOF transmission flexure system

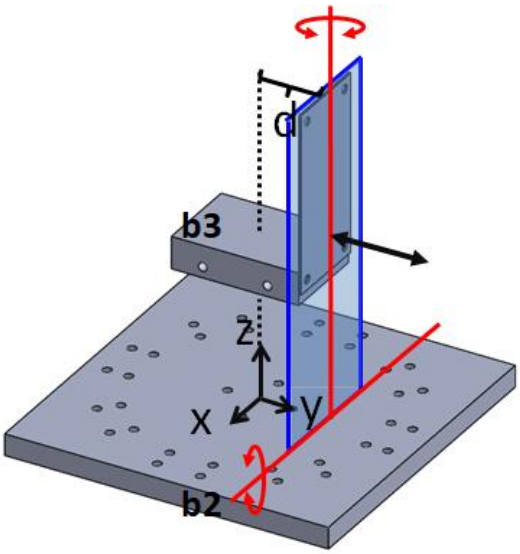

Figure 4.6: Implementation of $[jft]_{e2}$ of a 1 DOF transmission flexure system

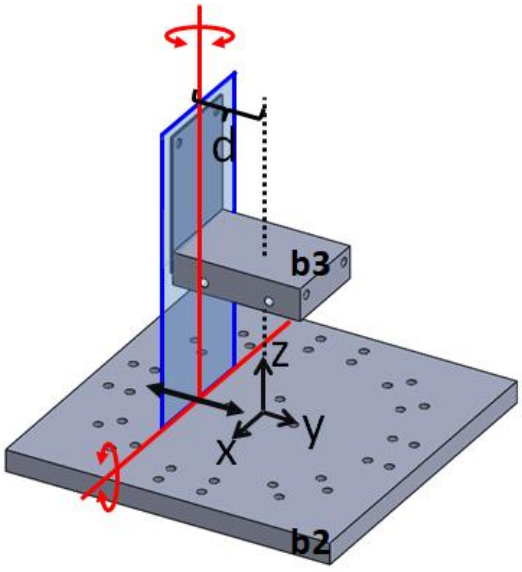

Figure 4.7: Implementation of $[jft]_{e4}$ of a 1 DOF transmission flexure system

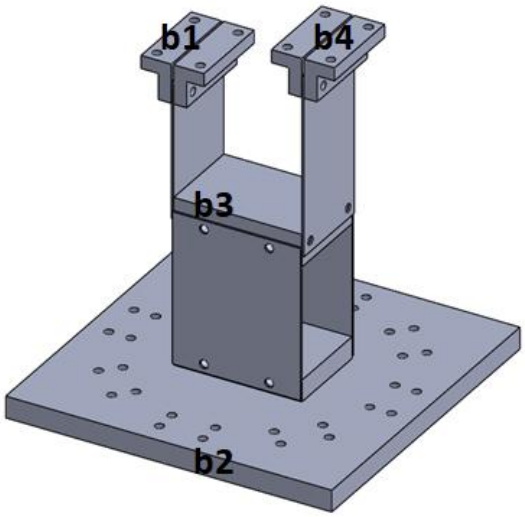

Figure 4.8: Placement of the flexures of *e2*, *e4* and *e5* of a 1 DOF transmission flexure system

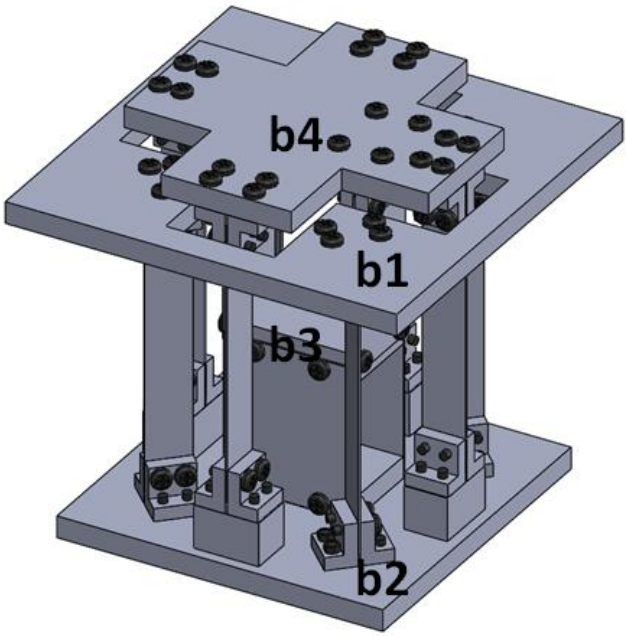

Figure 4.9: Design of a 1 DOF transmission flexure system

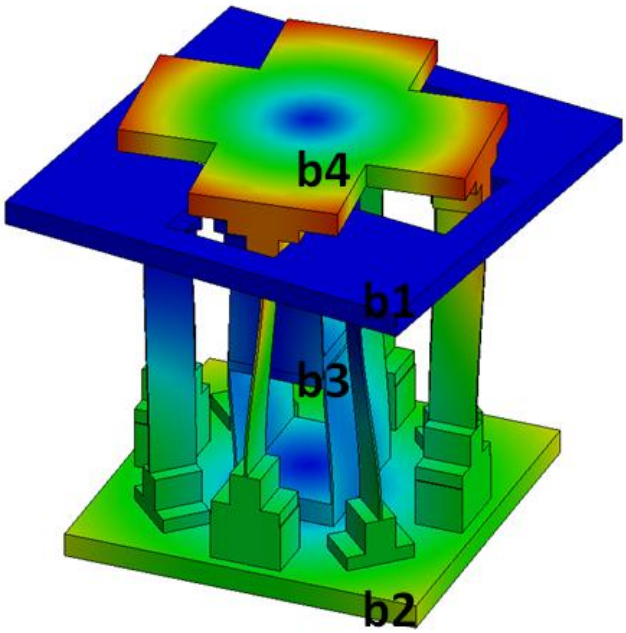

Figure 4.10: First natural frequency modeshape of a 1 DOF transmission flexure system

Alternative design: Suppose a system with the same transmission function but more planes of symmetry is desired. To synthesize such a system, the same graph in Fig 4.1 is chosen since it is the simplest graph and step one through four is repeated. Different design choices than the previous design are made at the start of step 5, and different set of possible solutions are obtained and shown in table 4.1. Interpreting the twist vectors, $[jft]_{e1}$ and $[jft]_{e3}$ are rotations about the z-axis same as the previous design, and ide achieved by sets of blade flexures intersecting at the z-axis shown in Fig. 4.11 and Fig. 4.12. Also the same as the previous design, the flexures of *e1* and *e3* are connected in serial as shown in Fig. 4.13. The two rotations and one translation of $[jft]_{e2}$ is achieved by 6 wire flexures linearly combining their constraining action into the a blue plane and implemented as a blade flexure as shown in Fig. 4.14. According to FACT, $[jft]_{e4}$ and $[jft]_{e5}$ are implemented as two sets of

Edge	Joint freedom topology matrix $[jft]_{ei}$	Magnitude matrix $\mathbf{x_i}$
e1	$[jft]_{e1} = \begin{bmatrix} 0 \\ 0 \\ 1 \\ 0 \\ 0 \\ 0 \end{bmatrix}$	$\mathbf{x}_1 = 1$
e2	$[jft]_{e2} = \begin{bmatrix} 0 & 1 & 0 \\ 0 & 0 & 1 \\ 0 & 0 & 0 \\ 0 & 0 & 0 \\ 0 & 0 & 0 \\ 1 & 0 & 0 \end{bmatrix}$	$\mathbf{x}_2 = \begin{bmatrix} p_1 \\ 0 \\ 0 \end{bmatrix}$
e3	$[jft]_{e3} = \begin{bmatrix} 0 \\ 0 \\ 1 \\ 0 \\ 0 \\ 0 \end{bmatrix}$	$\mathbf{x}_1 = 1$
e4	$[jft]_{e4} = \begin{bmatrix} 0 & 1 & 0 \\ 0 & 0 & 1 \\ 1 & 0 & 0 \\ 0 & 2p_2 & 0 \\ 0 & 0 & 2p_2 \\ \frac{p_1}{2} & 0 & 0 \end{bmatrix}$	$\mathbf{x}_4 = \begin{bmatrix} -2 \\ 0 \\ 0 \end{bmatrix}$
e5	$[jft]_{e5} = \begin{bmatrix} 0 & 1 & 0 \\ 0 & 0 & 1 \\ 1 & 0 & 0 \\ 0 & p_2 & 0 \\ 0 & 0 & p_2 \\ p_1 & 0 & 0 \end{bmatrix}$	$\mathbf{x}_5 = \begin{bmatrix} -1 \\ 0 \\ 0 \end{bmatrix}$

Table 4.1: Joint freedom topology matrices for a 1 DOF transmission flexure system

wire flexures arranged to form two separate circular hyperboloid centered around the z-axis as shown

in Fig. 4.15 and Fig. 4.16, where each set of circular hyperboloid allows three screw motion DOFs, represented by green lines, listed in table 4.1. Note that in table 4.1, only the twist vectors in the first column of $[jft]_{e4}$ and $[jft]_{e5}$ has a non-zero magnitude, and they are the screw motions allowed by the system in this design, the rest of the screws are inactive for this example. The placement of the flexures of *e2*, *e4* and *e5* is shown in Fig. 4.17. The complete design is shown in Fig. 4.18.

Frequency modal analysis is performed with SOLIDWORKS to validate the design. The first natural frequency modeshape is as shown in Fig. 4.19. The FEA results confirm that the stage rotates twice as much as the input body.

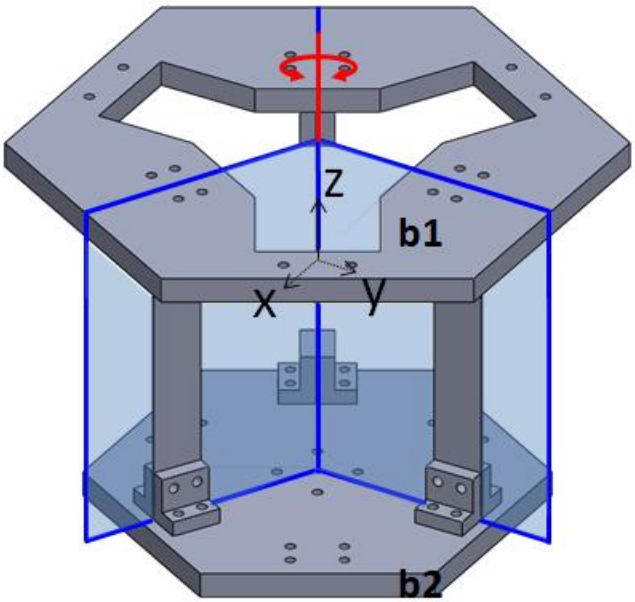

Figure 4.11 Implementation of $[jft]_{e1}$ of a 1 DOF transmission flexure system

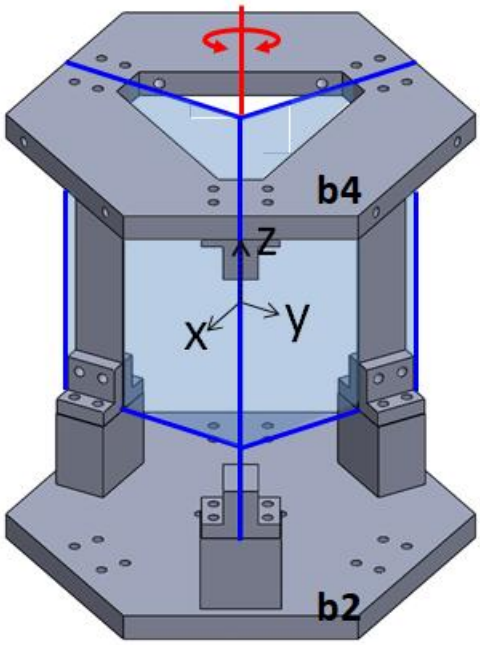

Figure 4.12 Implementation of $[jft]_{e3}$ of a 1 DOF transmission flexure system

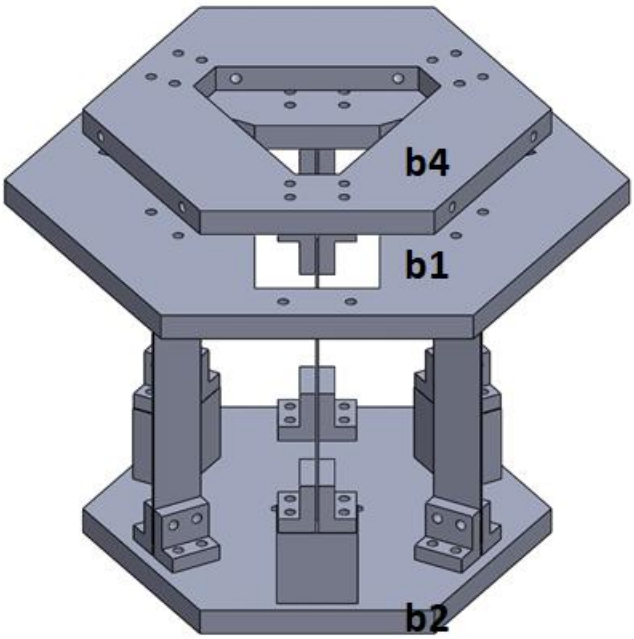

Figure 4.13: Placement of the flexures for *e1* and *e3* of a 1 DOF transmission flexure system

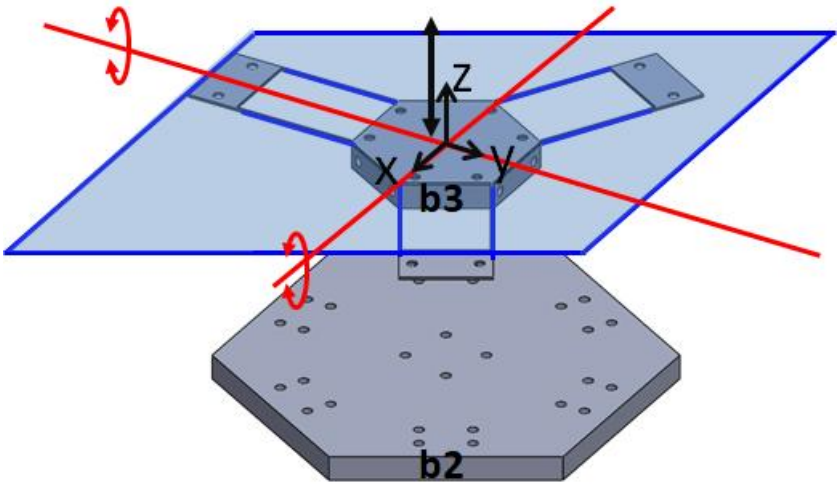

Figure 4.14 Implementation of $[jft]_{e2}$ of a transmission flexure system

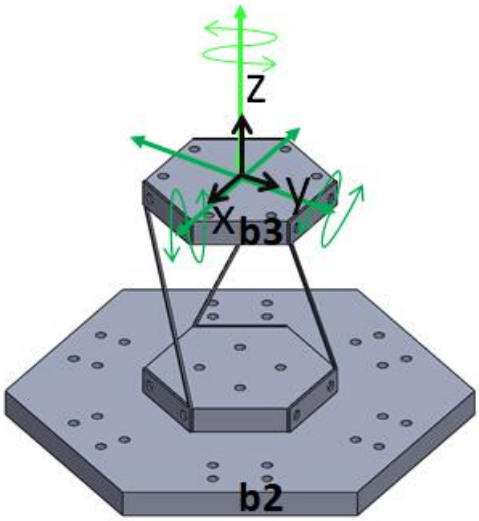

Figure 4.15 Implementation of $[jft]_{e5}$ of a transmission flexure system

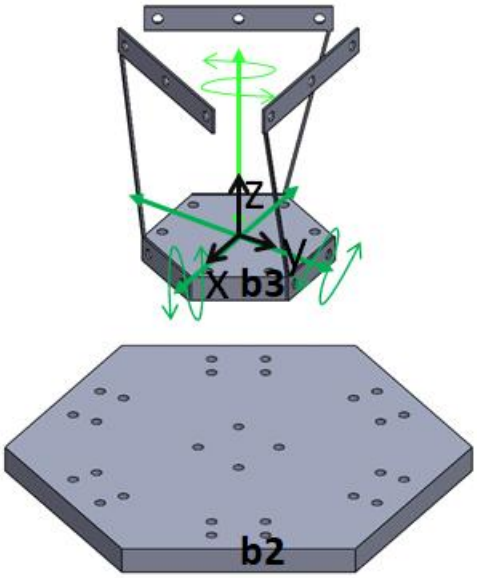

Figure 4.16 Implementation of $[jft]_{e4}$ of a transmission flexure system

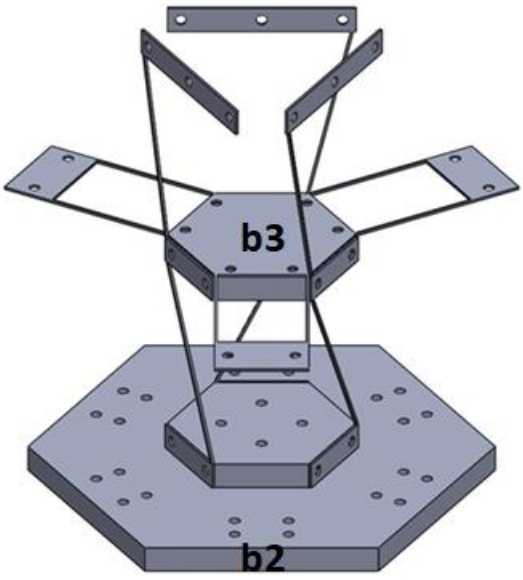

Figure 4.17: Placement of flexures of *e2*, *e4* and *e5* of a transmission flexure system

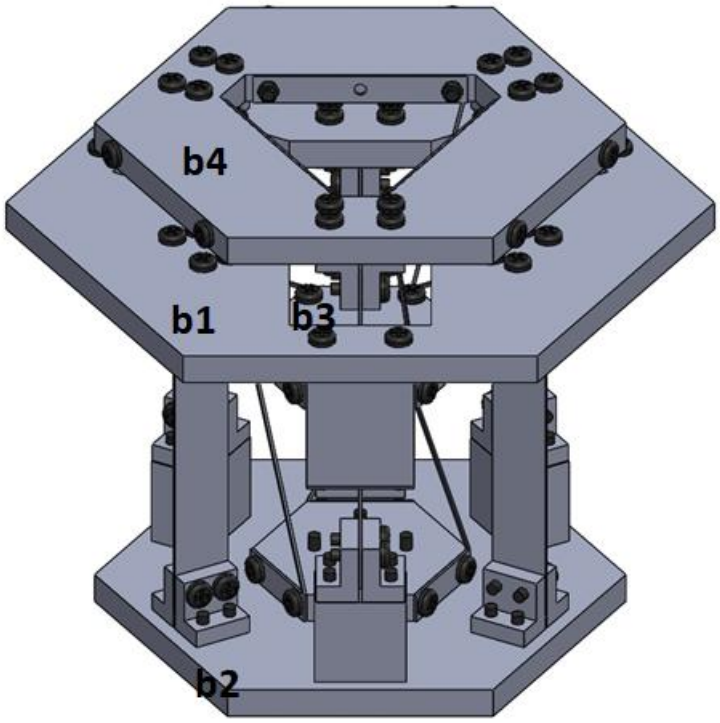

Figure 4.18: Design of a 1 DOF transmission flexure system

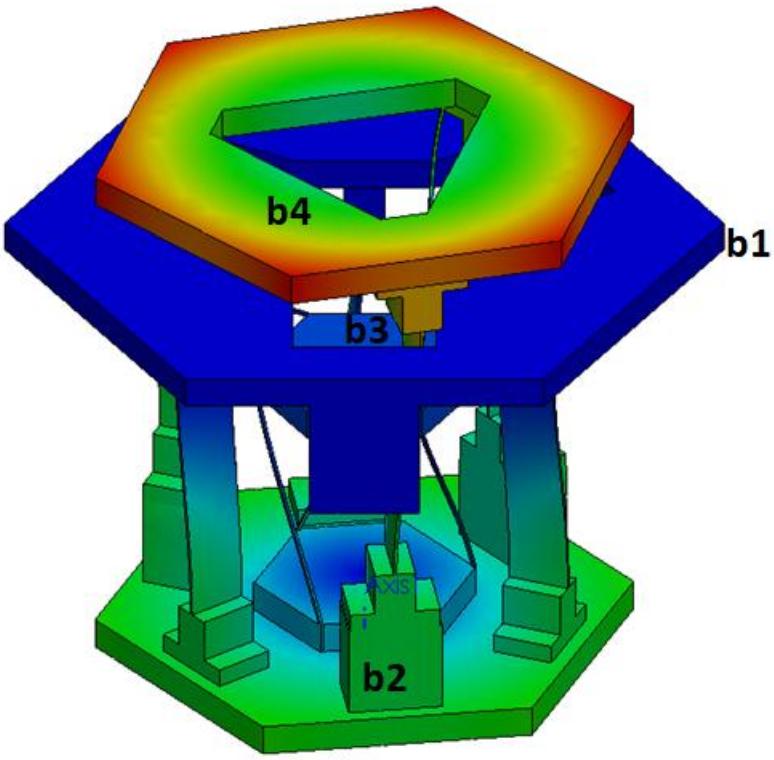

Figure 4.19: First natural frequency modeshape of a 1 DOF transmission flexure system

4.2 Case study 2: **Design of a transmission flexure system that doubles three DOFs of motion**

Suppose that in a similar Cartesian coordinates frame, three DOFs of motion are given as the input, a rotation parallel to the z-axis, a translation in the x-direction, and a translation in the y-direction. The desired outputs are the same three directions of motion with twice the magnitude. A flexure system that achieves the described function can also be designed using the same six-step approach introduced in this section.

Step 1: Identify desired motion and design requirements. The desired input and output motions are classified as 3 DOF type 2 in the FACT library in Fig. 1.3. The twist vectors for the input are interpreted according to

$$\mathbf{T}_{\mathbf{input}} = \begin{bmatrix} 0 & 0 & 0 \\ 0 & 0 & 0 \\ \omega_1 & 0 & 0 \\ 0 & v_1 & 0 \\ 0 & 0 & v_2 \\ 0 & 0 & 0 \end{bmatrix} \tag{4.13}$$

and twist vectors for the output interpreted according to

$$\mathbf{T}_{\mathbf{output}} = \begin{bmatrix} 0 & 0 & 0 \\ 0 & 0 & 0 \\ 2\omega_1 & 0 & 0 \\ 0 & 2v_1 & 0 \\ 0 & 0 & 2v_2 \\ 0 & 0 & 0 \end{bmatrix} \tag{4.14}$$

Step 2: Choose a Graph. The same graph shown in Fig. 4.1 is chosen for this case study, where *b1* is the ground, *b2* the input, and *b4* is the output stage.

Step 3: Construct the governing equation [FT][X] = 0. The graph chosen in Fig. 4.1 yields the governing equation of:

$$[\mathbf{FT}][\mathbf{X}] = \begin{bmatrix} [jft]_{e1} & -[jft]_{e2} & 0 & 0 & [jft]_{e5} \\ 0 & 0 & [jft]_{e3} & -[jft]_{e4} & -[jft]_{e5} \end{bmatrix} \begin{bmatrix} \mathbf{x_1} \\ \mathbf{x_2} \\ \mathbf{x_3} \\ \mathbf{x_4} \\ \mathbf{x_5} \end{bmatrix} = 0 \tag{4.15}$$

where $[jft]_{ei}$ correspond to edge *i*, and their placement is determined by visual inspection of independent loops in the graph of Fig. 4.1. The number of column in the [**X**] matrix is the number of DOF in the system, which equals to 3 to achieve the transmission of all three DOFs.

Step 4: Interpret the desired motion as components of the governing equation. Similar to the previous case study, the path from the ground to input goes through edge *e1* of the graph in Fig. 4.1. To allow the input motion, a solution set for the flexure of *e1* is

$$[jft]_{e1}\mathbf{x}_1 = \begin{bmatrix} 0 & 0 & 0 \\ 0 & 0 & 0 \\ 1 & 0 & 0 \\ 0 & 1 & 0 \\ 0 & 0 & 1 \\ 0 & 0 & 0 \end{bmatrix} \begin{bmatrix} 1 \\ 1 \\ 1 \end{bmatrix} \tag{4.16}$$

A path can be traced from the ground to the output through *e1* and *e3*, in order to satisfy the output having twice the magnitude, the following relation is obtained:

$$[jft]_{e1}\mathbf{x}_1 + [jft]_{e3}\mathbf{x}_3 = \begin{bmatrix} 0 & 0 & 0 \\ 0 & 0 & 0 \\ 2 & 0 & 0 \\ 0 & 2 & 0 \\ 0 & 0 & 2 \\ 0 & 0 & 0 \end{bmatrix} \tag{4.17}$$

which yields the solution set of the flexures of *e3* to be

$$[jft]_{e3}\mathbf{x}_3 = \begin{bmatrix} 0 & 0 & 0 \\ 0 & 0 & 0 \\ 1 & 0 & 0 \\ 0 & 1 & 0 \\ 0 & 0 & 1 \\ 0 & 0 & 0 \end{bmatrix} \begin{bmatrix} 1 \\ 1 \\ 1 \end{bmatrix} \tag{4.18}$$

Step 5: Find possible solutions to the governing equation. Substitute $[jft]_{e1}$, $[jft]_{e3}$, $\mathbf{x_1}$,and $\mathbf{x_3}$ into [**FT**] and [**X**] matrices into the governing equation, the set of chosen solutions are shown in Table. 4.2.

Step 6: Interpret joint freedom topology matrices as flexure elements or flexure subsystems using FACT. According to FACT, the two translations and one rotation of both $[jft]_{e1}$ and $[jft]_{e3}$ can be implemented with wire flexures parallel to each other but not all occupying the same plane as shown

Edge	Joint freedom topology matrix $[jft]_{ei}$	Magnitude matrix $\mathbf{x_i}$

e1	$[jft]_{e1} = \begin{bmatrix} 0 & 0 & 0 \\ 0 & 0 & 0 \\ 1 & 0 & 0 \\ 0 & 1 & 0 \\ 0 & 0 & 1 \\ 0 & 0 & 0 \end{bmatrix}$	$\mathbf{x}_1 = \begin{bmatrix} 1 \\ 1 \\ 1 \end{bmatrix}$
e2	$[jft]_{e2} = \begin{bmatrix} 0 & 1 & 0 \\ 0 & 0 & 1 \\ 0 & 0 & 0 \\ 0 & 0 & 0 \\ 0 & 0 & 0 \\ 1 & 0 & 0 \end{bmatrix}$	$\mathbf{x}_2 = \begin{bmatrix} p_1 \\ -\frac{1}{p_2} \\ -\frac{1}{p_2} \end{bmatrix}$
e3	$[jft]_{e3} = \begin{bmatrix} 0 & 0 & 0 \\ 0 & 0 & 0 \\ 1 & 0 & 0 \\ 0 & 1 & 0 \\ 0 & 0 & 1 \\ 0 & 0 & 0 \end{bmatrix}$	$\mathbf{x}_3 = \begin{bmatrix} 1 \\ 1 \\ 1 \end{bmatrix}$
e4	$[jft]_{e4} = \begin{bmatrix} 0 & 1 & 0 \\ 0 & 0 & 1 \\ 1 & 0 & 0 \\ 0 & 2p_2 & 0 \\ 0 & 0 & 2p_2 \\ \frac{p_1}{2} & 0 & 0 \end{bmatrix}$	$\mathbf{x}_4 = \begin{bmatrix} -2 \\ 0 \\ 0 \end{bmatrix}$
e5	$[jft]_{e5} = \begin{bmatrix} 0 & 1 & 0 \\ 0 & 0 & 1 \\ 1 & 0 & 0 \\ 0 & p_2 & 0 \\ 0 & 0 & p_2 \\ p_1 & 0 & 0 \end{bmatrix}$	$\mathbf{x}_5 = \begin{bmatrix} -1 \\ 0 \\ 0 \end{bmatrix}$

Table 4.2: Joint freedom topology matrices for the a 3 DOF transmission flexure system

in Fig. 4.20 and Fig. 4.21. The motion of $[jft]_{e2}$ is achieved by 6 wire flexures linearly combining into the a constraint space same as the 1 DOF design previously shown in Fig. 4.14. The motion of both

$[jft]_{e4}$ and $[jft]_{e5}$ can be achieved by two sets of wire flexures arranged to form two separate circular hyperboloids the same as the 1 DOF design previously shown in Fig. 4.15 and Fig. 4.16. Connecting all the subsystems, the final flexure design is shown in Fig. 4.22.

Frequency modal analysis is performed with SOLIDWORKS to validate the design. The first three natural frequency modeshapes are as shown in Fig. 4.23 to Fig. 4.25. The FEA results confirm that the output body *b4* moves twice as much as the input body *b2* for all first three modeshapes.

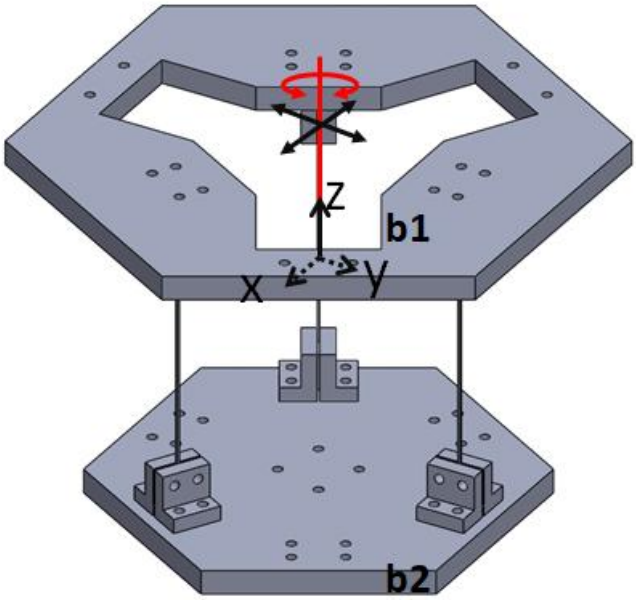

Figure 4.20 Implementation of $[jft]_{e1}$ of a 3 DOF transmission flexure system

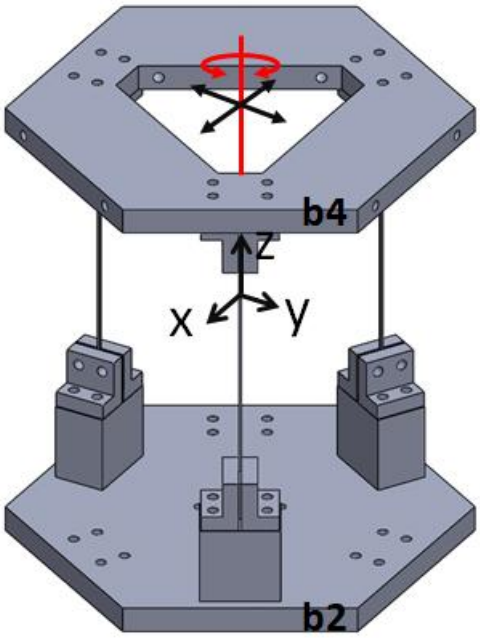

Figure 4.21 Implementation of $[jft]_{e3}$ of a 3 DOF transmission flexure system

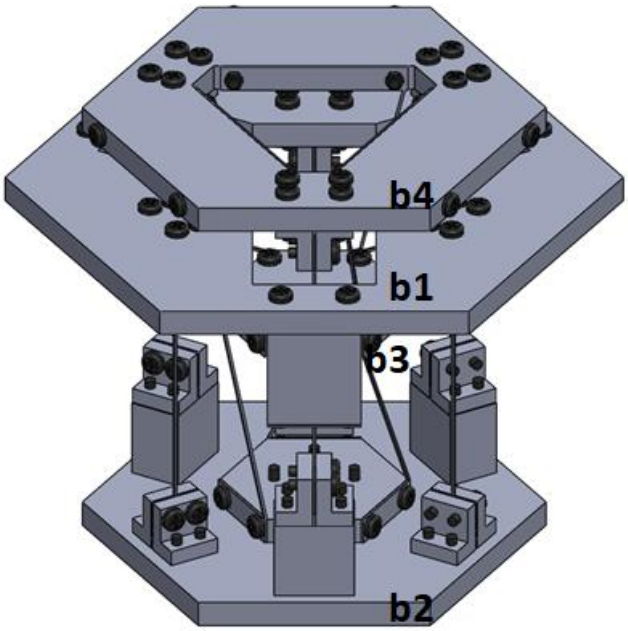

Figure 4.22: Design of a 3 DOF transmission flexure system

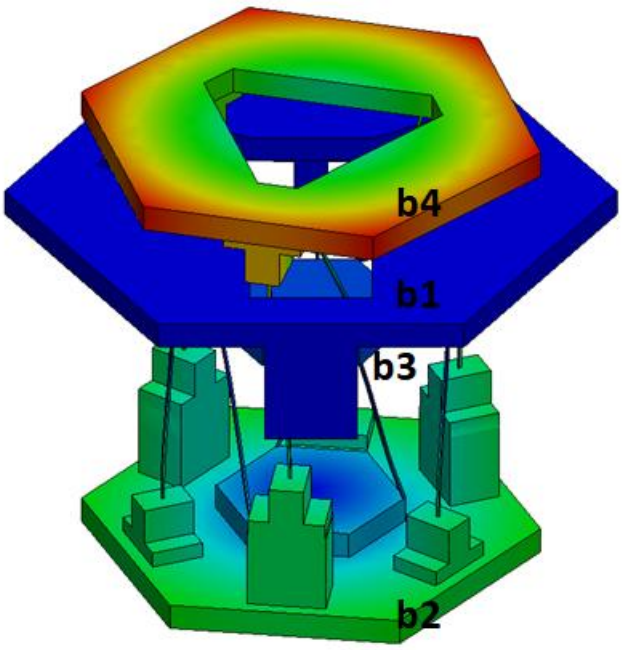

Figure 4.23: First natural frequency modeshape of a 3 DOF transmission flexure system

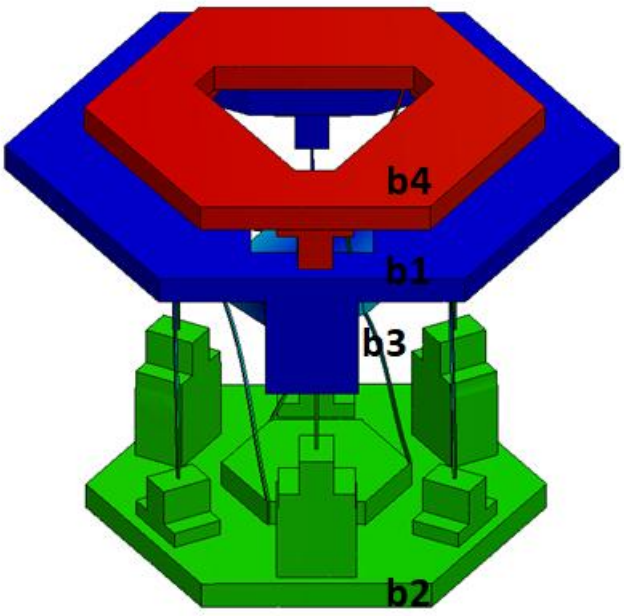

Figure 4.24: Second natural frequency modeshape of a 3 DOF transmission flexure system

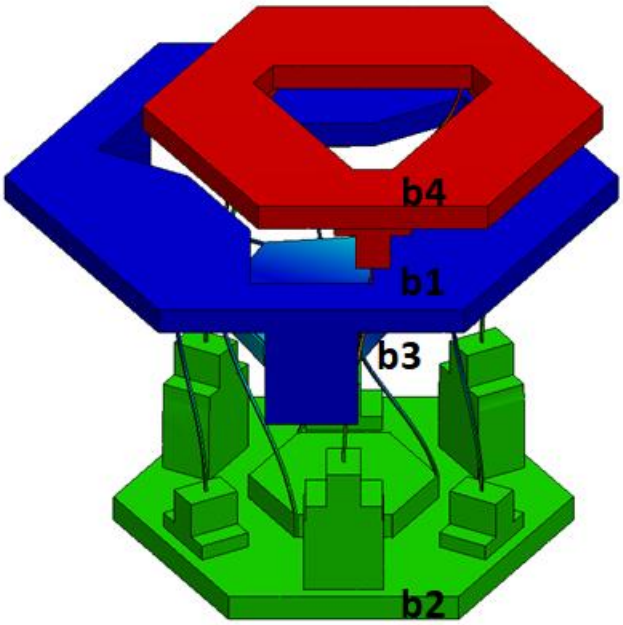

Figure 4.25: Third natural frequency modeshape of a 3 DOF transmission flexure system

4.3 Case study 3: Design of a negative Poisson's ratio microarchitectured material

Suppose a negative Poisson's microarchitectured material lattice is desired. Negative Poisson's ratio is achieved for a unit cell if one surface of the unit cell is pushed in or pulled out, all other surfaces of the unit cell should contract inwards or expands outwards respectively. The motion of a negative Poisson's ratio unit cell can therefore be considered as a flexure transmission system with an input of a pure translation and an output of a pure translation in the desired direction. A flexure system with the aforementioned input and output motion can be synthesized with the same method introduced in previous sections of this chapter.

For this case study, a highly symmetric design is preferred, and the design process is simplified by only designing a part of the system, and then the partially-completed system is mirrored about the

various planes of symmetry into a full design. The same six-step synthesis process for the partial system is presented as follows:

Step 1: Identify desired motion and design requirements. A coordinates system is set at the center of the unit cell, the input then can be interpreted as a translation in the positive x-direction, i.e. $[0 \quad 0 \quad 0 \quad v \quad 0 \quad 0]^T$, and the output can be interpreted as a translation in the positive y-direction, i.e. $[0 \quad 0 \quad 0 \quad 0 \quad v \quad 0]^T$. In addition to the desired motions, a highly symmetric design is preferred, and should be kept in mind when selecting the system graph and flexure elements later in the synthesis process.

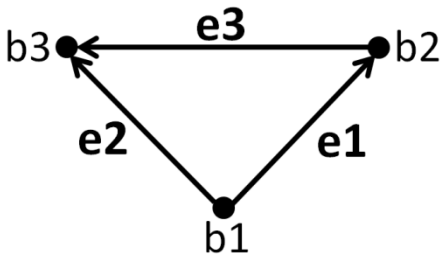

Figure 4.26: System graph for partial design of a negative Poisson's ratio microarchitectured material

Step 2: Choose a Graph. The graph chosen is shown in Fig.4.26. It is the simplest graph containing only the fixed ground *b1*, the input *b2*, and the output *b3*. The graph is symmetric about *b1*, allowing a symmetric design.

Step 3: Construct the governing equation [FT][X] = 0. The graph chosen in Fig. 4.26 yields the governing equation of:

$$[\mathbf{FT}][\mathbf{X}] = [[jft]_{e1} \quad [jft]_{e2} \quad -[jft]_{e3}] \begin{bmatrix} \mathbf{x_1} \\ \mathbf{x}_2 \\ \mathbf{x}_3 \end{bmatrix} = 0 \tag{4.19}$$

where $[jft]_{ei}$ correspond to edge *i*, and the number of column in the [**X**] matrix is one since the system is of 1 DOF.

Step 4: Interpret the desired motion as components of the governing equation. The input body is connected directly to the ground through *e1*, for the desired motion identified in step one, the simplest interpretation of *e1* is $[jft]_{e1} = [0 \quad 0 \quad 0 \quad 1 \quad 0 \quad 0]^T$ and $\mathbf{x_1}$ = 1. Likewise, since the output is directly to the ground through *e3*, and the simplest interpretation of e1 is $[jft]_{e1} = [0 \quad 0 \quad 0 \quad 0 \quad 1 \quad 0]^T$ and $\mathbf{x_3}$ = 1.

Step 5: Find possible solutions to the governing equation. Substitute $[jft]_{e1}$, $[jft]_{e3}$, $\mathbf{x_1}$,and $\mathbf{x_3}$ into [**FT**] and [**X**] matrices into the governing equation and solve for a compatible $[jft]_{e2}$. The solution set chosen solution for *e2* is defined according to

$$[jft]_{e2}\mathbf{x}_2 = \begin{bmatrix} 0 & 1 & 0 & 0 \\ 0 & 1 & 0 & 0 \\ 0 & 0 & 1 & 0 \\ -1 & 0 & 0 & 0 \\ 1 & 0 & 0 & 0 \\ 0 & 0 & 0 & 1 \end{bmatrix} \begin{bmatrix} 1 \\ 0 \\ 0 \\ 0 \end{bmatrix} \tag{4.20}$$

The solution is selected for being able to be implemented as a symmetric design.

Step 6: Interpret joint freedom topology matrices as flexure elements or flexure subsystems using FACT. For this example, the freedom and constraint space of $[jft]_{e1}$ and $[jft]_{e3}$ are a black arrow and sets of parallel blue planes respectively, and can be achieved by sets of parallel blade flexures as shown in Fig. 4.27 and Fig. 4.28. The freedom and constraint space for $[jft]_{e2}$ is of 4 DOF type 2 in the FACT library of Fig. 1.3. The freedom space allows two rotational and two translational DOFs, and the constraint space contains a plane of parallel blue lines. The flexure subsystem for *e2* implemented as a set of two bent blades shown in Fig. 4.29, which is kinematically equivalent to two wire flexures located at the fold of the blade flexures. Connecting all the flexure elements, the transmission flexure is as shown in Fig. 4.30.

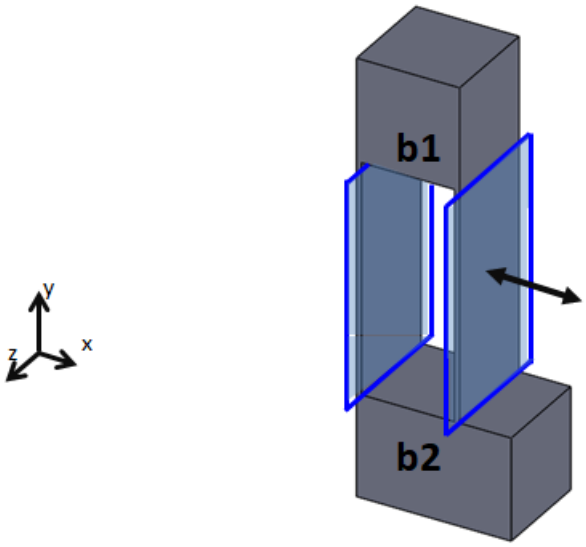

Figure 4.27 Implementation of $[jft]_{e1}$ of a negative Poisson's ratio microarchitectured material

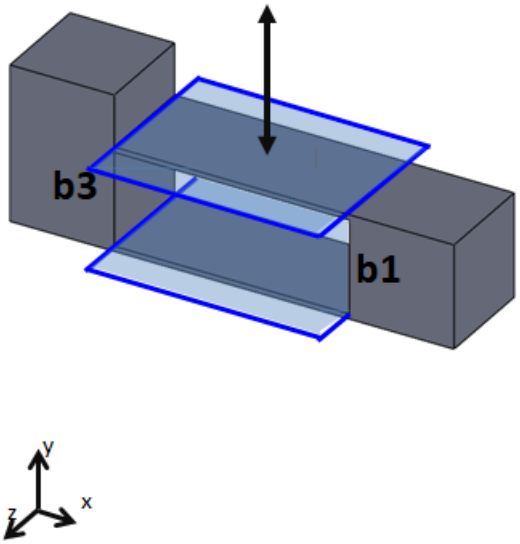

Figure 4.28 Implementation of $[jft]_{e3}$ of a negative Poisson's ratio microarchitectured material

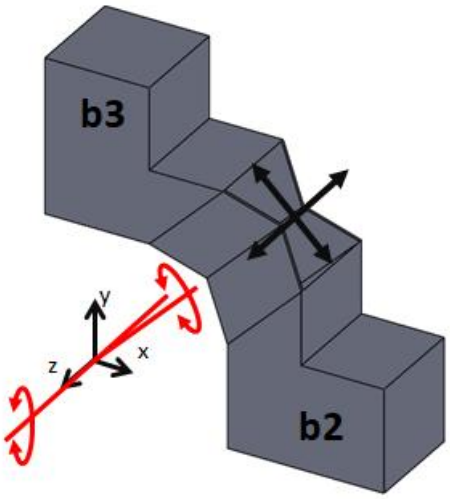

Figure 4.29 Implementation of $[jft]_{e2}$ of a negative Poisson's ratio microarchitectured material

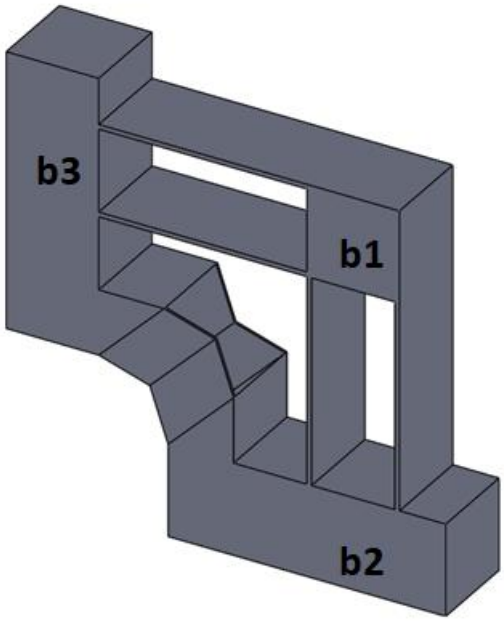

Figure 4.30 A corner of a negative Poisson’s ratio microarchitectured material

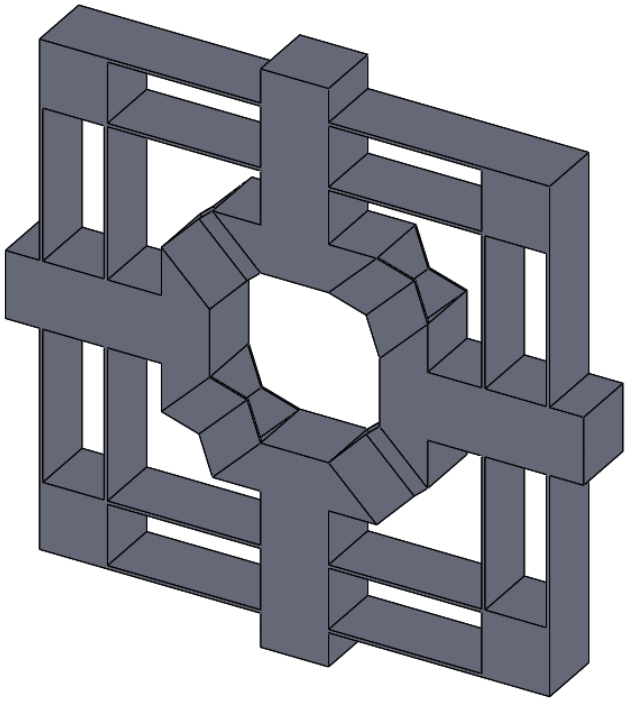

Figure 4.31 Cross-section of a negative Poisson’s ratio microarchitectured material

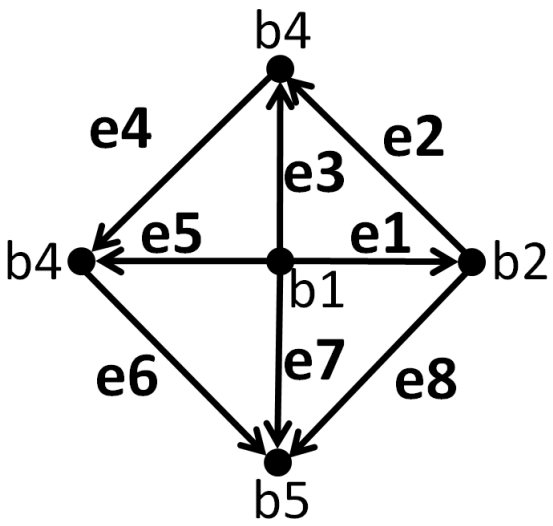

Figure 4.32 System graph of cross-section of a negative Poisson's ratio microarchitectured material

Using the partial design to construct the full design, the 2D cross-section of the entire negative Poisson's ratio microarchitectured material design is shown in Fig. 4.31. The graph for the 2D cross-section is as shown in Fig. 4.32, and its corresponding [**FT**] is

$$[\mathbf{FT}]=\begin{bmatrix} [jft]_{e1} & [jft]_{e2} & -[jft]_{e3} & 0 & 0 & 0 & 0 & 0 \\ 0 & 0 & [jft]_{e3} & [jft]_{e4} & -[jft]_{e5} & 0 & 0 & 0 \\ 0 & 0 & 0 & 0 & [jft]_{e5} & [jft]_{e6} & -[jft]_{e7} & 0 \\ -[jft]_{e1} & 0 & 0 & 0 & 0 & 0 & [jft]_{e7} & -[jft]_{e8} \end{bmatrix} \quad (4.21)$$

The complete 3D design is as shown in Fig. 4.33. The graph for the 3D design is as shown in Fig. 4.34, and its corresponding [**FT**] is:

$$[\mathbf{FT}]=\begin{bmatrix}
[jft]_{e1} & [jft]_{e2} & -[jft]_{e3} & 0 & 0 & 0 & 0 & 0 & 0 & 0 & 0 & 0 & 0 & 0 & 0 & 0 \\
0 & 0 & [jft]_{e3} & [jft]_{e4} & -[jft]_{e5} & 0 & 0 & 0 & 0 & 0 & 0 & 0 & 0 & 0 & 0 & 0 \\
0 & 0 & 0 & 0 & [jft]_{e5} & [jft]_{e5} & [jft]_{e5} & 0 & 0 & 0 & 0 & 0 & 0 & 0 & 0 & 0 \\
0 & 0 & 0 & 0 & 0 & 0 & [jft]_{e7} & [jft]_{e8} & -[jft]_{e9} & 0 & 0 & 0 & 0 & 0 & 0 & 0 \\
0 & 0 & 0 & 0 & 0 & 0 & 0 & 0 & [jft]_{e9} & [jft]_{e10} & -[jft]_{e11} & 0 & 0 & 0 & 0 & 0 \\
0 & 0 & 0 & 0 & 0 & 0 & 0 & 0 & 0 & 0 & [jft]_{e11} & [jft]_{e12} & -[jft]_{e13} & 0 & 0 & 0 \\
0 & 0 & 0 & 0 & 0 & 0 & 0 & 0 & 0 & 0 & 0 & 0 & [jft]_{e13} & [jft]_{e14} & -[jft]_{e15} & 0 \\
-[jft]_{e1} & 0 & 0 & 0 & 0 & 0 & 0 & 0 & 0 & 0 & 0 & 0 & 0 & 0 & [jft]_{e15} & [jft]_{e16}
\end{bmatrix}$$

(4.22)

Even though the more complex graphs and [**FT**] seemed intimidating, the same synthesis process can still be applied to obtain the same design.

Frequency modal analysis is performed with SOLIDWORKS to validate the design. The first natural frequency modeshapes of the 2D cross section is shown in Fig. 4.35, and the first natural frequency modeshapes of the complete 3D design is shown in Fig. 4.36.

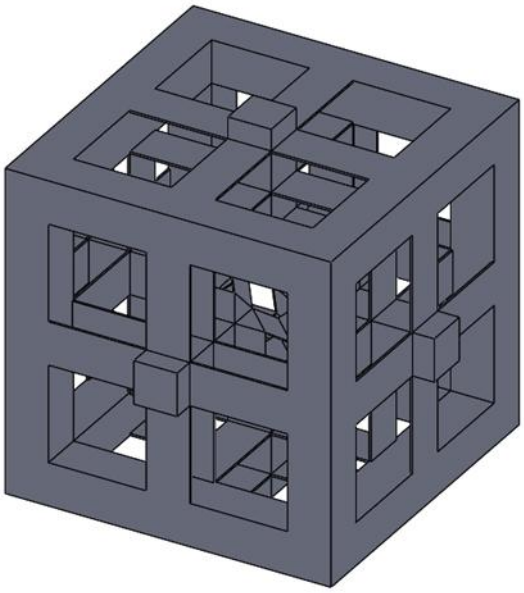

Figure 4.33 Design of a negative Poisson's ratio microarchitectured material

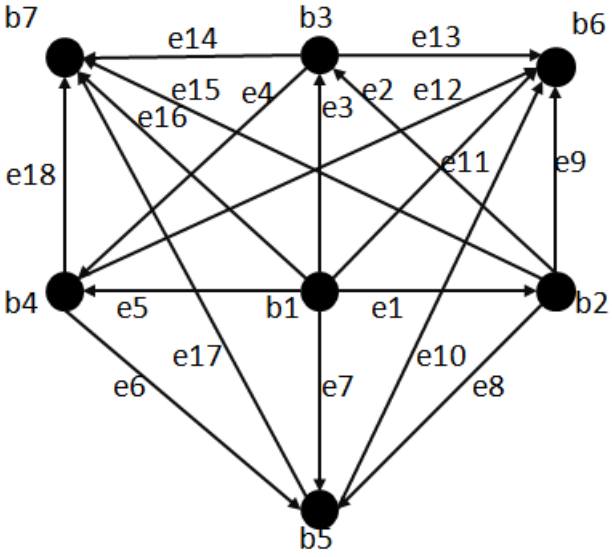

Figure 4.34 System graph of a negative Poisson's ratio microarchitectured material

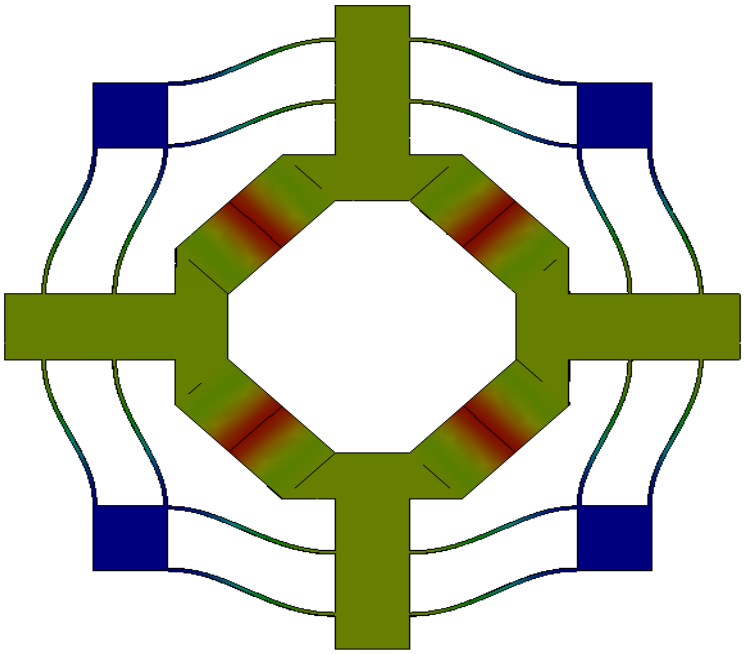

Figure 4.35 First natural frequency modeshape of the cross section of a negative Poisson's ratio microarchitectured material

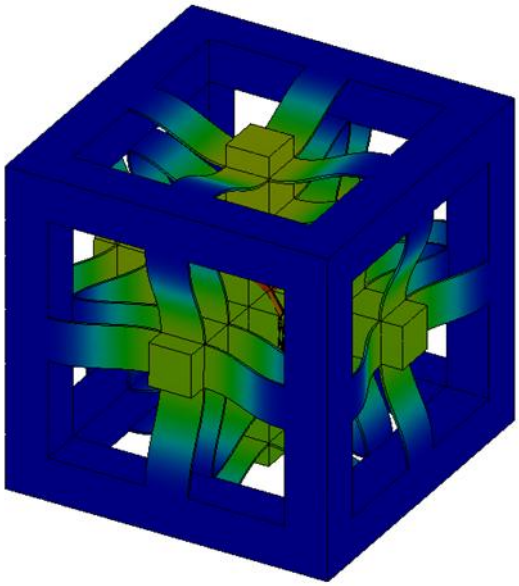

Figure 4.36 First natural frequency modeshape of a negative Poisson's ratio microarchitectured material

Alternative design: Here two alternative designs of the negative Poisson's ratio microarchitectured material are presented. The same synthesis process is applied, and a transmission flexure is first designed as a corner of the microarchitectured material. The graph chosen for the transmission flexure is shown in Fig. 4.37, defining the governing equation according to

$$[\mathbf{FT}][\mathbf{X}] = \begin{bmatrix} [jft]_{e1} & -[jft]_{e2} & 0 & 0 & [jft]_{e5} \\ 0 & 0 & [jft]_{e3} & -[jft]_{e4} & -[jft]_{e5} \end{bmatrix} \begin{bmatrix} \mathbf{x_1} \\ \mathbf{x_2} \\ \mathbf{x_3} \\ \mathbf{x_4} \\ \mathbf{x_5} \end{bmatrix} = 0 \qquad (4.23)$$

The chosen solution set for Eq. (4.23) is shown in Table 4.3. The 2D cross-sections and one of the full 3D design is shown in Fig. 4.38 and Fig. 4.39. The 2D cross section and the full 3D design of the other design is shown in Fig. 4.40 and Fig. 4.41. Note that even though the two designs seems different, the flexure elements share the same [*jft*]s.

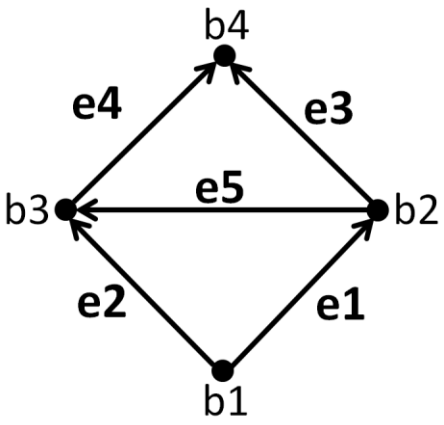

Figure 4.37 System graph for partial design of a negative Poisson's ratio microarchitectured material

Edge	Joint freedom topology matrix $[jft]_{ei}$	Magnitude matrix $\mathbf{x_i}$
e1	$[jft]_{e1} = \begin{bmatrix} 0 \\ 0 \\ 1 \\ 0 \\ 0 \\ 0 \end{bmatrix}$	$\mathbf{x}_1 = 1$
e2	$[jft]_{e2} = \begin{bmatrix} 0 & 0 \\ 0 & 0 \\ 0 & 1 \\ a & 0 \\ b & 0 \\ 0 & 0 \end{bmatrix}$	$\mathbf{x}_2 = \begin{bmatrix} \frac{-1}{(a-b)} \\ 0 \end{bmatrix}$
e3	$[jft]_{e3} = \begin{bmatrix} 0 \\ 0 \\ 1 \\ 0 \\ 0 \\ 0 \end{bmatrix}$	$\mathbf{x}_3 = 1$
e4	$[jft]_{e4} = \begin{bmatrix} 0 & 0 \\ 0 & 0 \\ 0 & 1 \\ b & 0 \\ a & 0 \\ 0 & 0 \end{bmatrix}$	$\mathbf{x}_4 = \begin{bmatrix} \frac{-1}{(a-b)} \\ 0 \end{bmatrix}$
e5	$[jft]_{e5} = \begin{bmatrix} 0 \\ 0 \\ 0 \\ 1 \\ 1 \\ 0 \end{bmatrix}$	$\mathbf{x}_5 = \frac{-b}{(a-b)}$

Table 4.3: Joint freedom topology matrices for a negative Poisson's ratio microarchitectured material

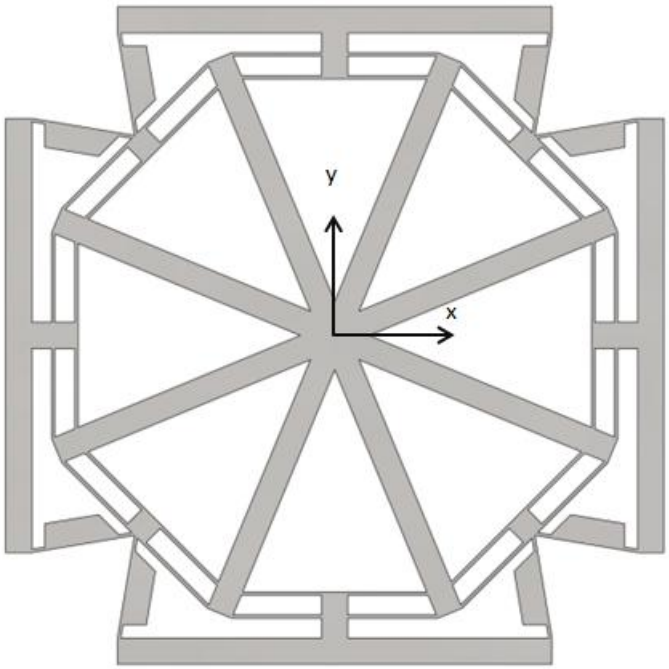

Figure 4.38 Cross section of a negative Poisson's ratio microarchitectured material

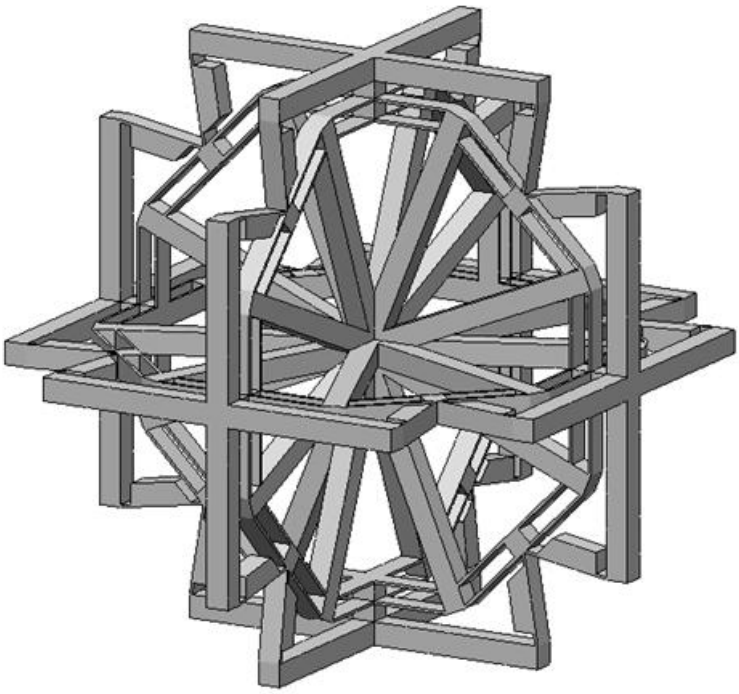

Figure 4.39 Design of a negative Poisson's ratio microarchitectured material

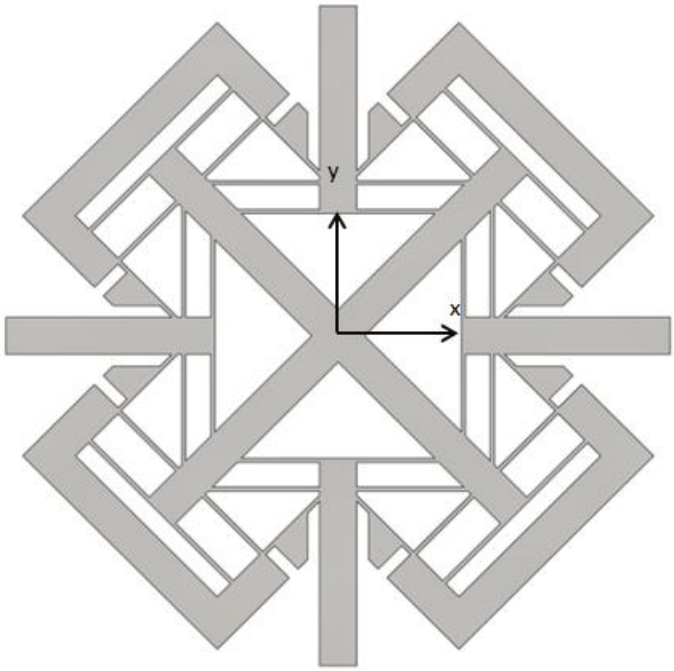

Figure 4.40 Cross section of a negative Poisson's ratio microarchitectured material

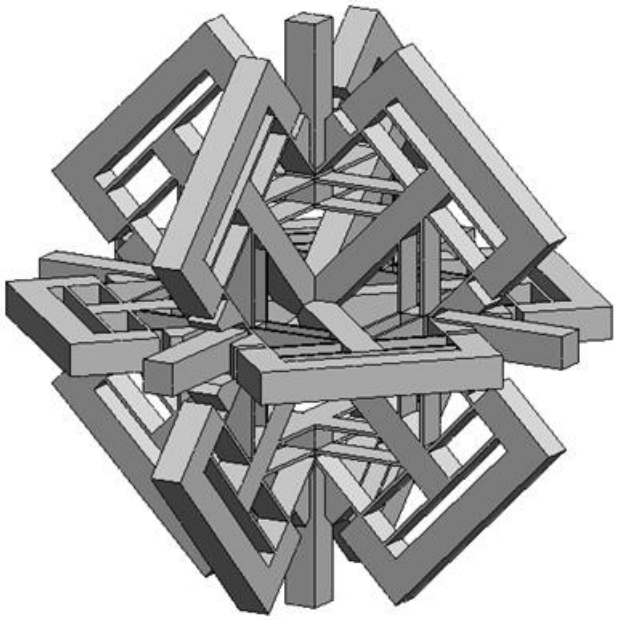

Figure 4.41 Design of a negative Poisson's ratio microarchitectured material

CHAPTER 5

Conclusion

In this thesis, systematic steps for both analysis and synthesis have been provided. The theory underlying these steps utilizes screw algebra, graph theory, and simple linear matrix-based calculations to rapidly determine the freedom spaces of thousands of rigid bodies that are joined together by compliant joints of any geometry.

The analysis approach enables automated mobility and constraint analysis of general flexure systems of any complexity including those classified as interconnected hybrid flexure systems. One can program a computer tool to automatically identify flexure elements and their constraint lines in a CAD model of a flexure system, then use the method developed in this thesis to solve for the freedom and constraint space of a designated body of the said flexure system. Principles of under-constraint and over-constraint are revised in the context of interconnected hybrid flexure systems and a case study is performed to demonstrate the theory's utility.

The synthesis approach enables the design of flexure systems of any complexity including those classified as interconnected hybrid flexure systems that cannot be designed via traditional freedom and constraint topology methods, allowing rapid conceptual design of many complex flexure systems such as flexure transmissions and microarchitectured materials.

The research in this work also laid a foundation to possible future advancements of an automated tool that allows more efficient enumeration of general flexure systems of any complexity.

References

[1] Smith, S. T., 2000, Flexures: Elements of elastic mechanisms, Gordon and Breach Science Publishers, Newark, N.J.

[2] Hopkins, J.B., 2013, "Designing Hybrid Flexure Systems and Elements Using Freedom and Constraint Topologies," *Mechanical Sciences*, 4, pp: 319-331.

[3] Panas, R.M., Hopkins, J.B., 2015, "Eliminating Underconstraint in Double Parallelogram Flexure Mechanisms," *Journal of Mechanical Design*, 137(9): 092301

[4] Valdevit, L., Jacobsen, J.A., Greer, J.R., Carter, W.B., 2011, "Protocols for the Optimal Design of Multi-functional Cellular Structures: From Hypersonics to Micro-Architectured Materials," *Journal of the American Ceramic Society*, 94:s15-s34.

[5] Deshpande, V.S., Fleck, N.A., Ashby, M.F., 2001, "Effective Properties of the Octet-truss Lattice Material," *Journal of the Mechanics and Physics of Solids*, 49(8):1747-1769

[6] Kadic, M., Bückmann, T., Stenger, N., Thiel, M., Wegener, M., 2012, "On the Practicability of Pentamode Mechanical Metamaterials," *Applied Physics Letters*, 100(19):191901.

[7] Lee, J., Kim, K., Ju, J., Kim, D., 2014, "Compliant Cellular Materials With Elliptical Holes for Extremely High Positive and Negative Poisson's Ratios," *Journal of Engineering Materials and Technology*, 137(1):011001-011001-17.

[8] Lakes, R.S., 1996, "Cellular Solid Structures With Unbounded Thermal Expansion," *Journal of Materials Science Letters*, 15(6):475-477.

[9] Ball, R.S., 1900, A Treatise on the Theory of Screws, Cambridge University Press, Cambridge, UK.

[10] Phillips, J., 1984, Freedom in Machinery: Volume 1, Introducing Screw Theory, Cambridge University Press, New York, NY.

[11] Murray, R.M., Li, Z., Sastry, S.S., 1994, A Mathematical Introduction to Robotic Manipulation, CRC Press LLC, Boca Raton, FL.

[12] Norman Biggs, 1974, Algebraic Graph Theory, Cambridge University Press.

[13] Leo J. Grady, Jonathan R. Polimeni, 2010, Discrete Calculus: Applied Analysis on Graphs for Computational Science, Springer London. pp. 44-48.

[14] Kong, X., Gosselin, C.M., 2007, Type Synthesis of Parallel Mechanisms, Springer Publishing Company

[15] Gibson, C.G., and Hunt, K.H., 1990, "Geometry of Screw Systems-I, Classification of Screw Systems," *Mechanisms and Machine Theory*, 25(1), pp: 1-10.

[16] Gibson, C.G., and Hunt, K.H., 1990, "Geometry of Screw Systems-II, Classification of Screw Systems," *Mechanisms and Machine Theory*, 25(1), pp: 11-27.

[17] Rico, J.M., and Duffy, J., 1992, "Classification of Screw Systems—I: One- and Two-Systems," *Mechanism and Machine Theory*, 27(4), pp: 459-470.

[18] Rico, J.M., and Duffy, J., 1992, "Classification of Screw Systems—II: Three-systems. *Mechanism and Machine Theory*," 27(4), pp: 471-490.

[19] Rico, J.M., and Duffy, J., 1992, "Orthogonal Spaces and Screw Systems," *Mechanism and Machine Theory*, 27(4), pp. 451-458.

[20] Mohamed, M. G. and Duffy, J., 1985, "A Direct Determination of the Instantaneous Kinematics of Fully Parallel Robot Manipulators," *Journal of Mechanisms Transmissions and Automation in Design*, 107(2), pp:226-229.

[21] Kumar, V., "Instantaneous Kinematics of Parallel-Chain Robotic Mechanisms," *Journal of Mechanical Design*, 114(3), pp:349-358.

[22] Kong, X., and Gosselin, C.M., 2004, "Type Synthesis of Three-Degree-of-Freedom Spherical Parallel Manipulators," *The International Journal of Robotics Research*, 23(3), pp: 237-245.

[23] Kong, X., and Gosselin, C.M., 2004, "Type Synthesis of 3-DOF Translational Parallel Manipulators Based on Screw Theory," *Journal of Mechanical Design*, 126(1), pp:83-92.

[24] Fang, Y., Tsai, L.W., 2002, “Structure Synthesis of a Class of 4-DoF and 5-DoF Parallel Manipulators with Identical Limb Structures,” *The International Journal of Robotics Research,* 21(9), pp:799-810.

[25] Freudenstein, F. and Dobrjanskyj, L., 1964, “On a theory for the type synthesis of mechanisms,” *Applied Mechanics: Proceedings of the Eleventh International Congress of Applied Mechanics Munich (Germany)*, pp. 420-428

[26] Dobrjanskyj, L. and Freudenstein, F.. 1967, “Some Applications of Graph Theory to the Structural Analysis of Mechanisms,” *Journal of Engineering for Industry* 89(1), 153-158

[27] Davies, T. 1981, “Kirchhoff's Circulation Law Applied to Multi-loop Kinematic Chains,” *Mechanism and Machine Theory*, 16(3), pp. 171-183.

[28] Angeles, J. and Gosselin, C.M., 1988, “Détermination du Degree de Liberté des Chaînes Cinématiques,” *Transactions of the Canadian Society for Mechanical Engineering*, 12(4) pp: 219–226

[29] Zoppi, M., Zlatanov, D., and Molfino, R., 2006, “On the velocity analysis of interconnected chains mechanisms,” *Mechanism and Machine Theory*, 41(11), pp: 1346-1358.

[30] Zeng, Q., Fang, Y., and Ehmann, K.F., 2011, “Design of a Novel 4-DOF Kinematotropic Hybrid Parallel Manipulator,” *Journal of Mechanical Design,* 133(12):121006.

[31] Lu, Y. and Leinonen, T., 2005 “Type synthesis of unified planar–spatial mechanisms by systematic linkage and topology matrix-graph technique” *Mechanism and Machine Theory,* 40(10), pp 1145-1163.

[32] Chen D.Z. and Yao, K.L., “Topological Synthesis of Fractionated Geared Differential Mechanisms,” *Journal of Mechanical Design,* 122(4), pp 472-478.

[33] Murphy, M. D., Midha, A., and Howell, L. L., 1996, “The Topological Synthesis of Compliant Mechanisms,” *Mechanism and Machine Theory*, 31(2) pp. 185-199.

[34] Pucheta,. A., and Cardona, A., 2010 “Design of bistable compliant mechanisms using precision-position and rigid-body replacement methods” *Mechanism and Machine Theory,* 45(2), pp: 304-326

[35] Merlet, J.P., 1989, "Singular Configurations of Parallel Manipulators and Grassmann Geometry," *The International Journal of Robotics Research*, 8(5): 45-56.

[36] Hao, F., McCarthy, J.M., 1998, "Conditions for Line-based Singularities in Spatial Platform Manipulators," *Journal of Robotic Systems*, 15(1): 43-55.

[37] Hopkins, J.B., 2007, "Design of Parallel Flexure Systems via Freedom and Constraint Topologies (FACT)." Master's Thesis. Massachusetts Institute of Technology.

[38] Hopkins, J.B., 2010, "Design of Flexure-Based Motion Stages for Mechatronic Systems via Freedom, Actuation and Constraint Topologies (FACT)." PhD Thesis. Massachusetts Institute of Technology.

[39] Hopkins, J.B., Culpepper, M.L., 2010, "Synthesis of Multi-degree of Freedom, Parallel Flexure System Concepts via Freedom and Constraint Topology (FACT)—Part I: Principles," *Precision Engineering*, 34(2): pp. 259-270.

[40] Su, H., Dorozhkin, D.V., Vance, J.M., 2009, "A Screw Theory Approach for the Conceptual Design of Flexible Joints for Compliant Mechanisms," *Journal of Mechanisms and Robotics*, 1(4), pp: 041009.

[41] Su, H., 2011, "Mobility Analysis of Flexure Mechanisms via Screw Algebra," J*ournal of Mechanisms and Robotics* 3(4): 0410

[42] Su, H. and Tari, H., 2011, "On Line Screw Systems and Their Application to Flexure Synthesis," *Journal of Mechanisms and Robotics*, 3(1): 011009

[43] Yu, J., Li, S., Su, H. and M. L. Culpepper, 2011, "Screw Theory Based Methodology for the Deterministic Type Synthesis of Flexure Mechanisms," *Journal of Mechanisms and Robotics*, 3(3): 031008

[44] Dai, J.S., Li, D., Zhang, Q., Jin, G., 2004, "Mobility analysis of a complex structured ball based on mechanism decomposition and equivalent screw system analysis," *Mechanism and Machine Theory*, 39(4), pp: 445-458

[45] Pham, H-H., Yeh, H-C., Chen, I-M., 2006, “Micromanipulation System Design Based on Selective Actuation Mechanisms,” *The International Journal of Robotics Research*, 25(2), pp: 171-186.

[46] Hao, G., Kong, X., 2013, “A Normalization-Based Approach to the Mobility Analysis of Spatial Compliant Multi-Beam Modules,” *Mechanism and Machine Theory*, 59, pp. 1-19.

[47] Zhang, Y., Su, H. J., and Liao, Q., 2014 “Mobility criteria of compliant mechanisms based on decomposition of compliance matrices,” *Mechanism and Machine Theory*, 79, pp. 80-93.

[48] Howell, L. L., 2001 Compliant Mechanisms. John Wiley & Sons, Inc., New York.

[49] Frecker MI, Ananthasuresh GK, Nishiwaki S, Kota S., 1997 “Topological Synthesis of Compliant Mechanisms Using Multi-Criteria Optimization” *Journal of Mechanical Design*, 119(2), pp: 238-245

[50] Cormen, T.H., Leiserson, C.E., Rivest, R.L., Stein, C., 2001, Introduction to Algorithms (second edition.). MIT Press and McGraw–Hill, pp: 595–601.

[51] Blanding, D.L., Exact Constraint: Machine Design Using Kinematic Principles. New York, NY: ASME Press, 1999.